

Precision measurement of the weak charge of the proton

The Jefferson Lab Q_{weak} Collaboration*

Large experimental programmes in the fields of nuclear and particle physics search for evidence of physics beyond that explained by current theories. The observation of the Higgs boson completed the set of particles predicted by the standard model, which currently provides the best description of fundamental particles and forces. However, this theory's limitations include a failure to predict fundamental parameters, such as the mass of the Higgs boson, and the inability to account for dark matter and energy, gravity, and the matter–antimatter asymmetry in the Universe, among other phenomena. These limitations have inspired searches for physics beyond the standard model in the post-Higgs era through the direct production of additional particles at high-energy accelerators, which have so far been unsuccessful. Examples include searches for supersymmetric particles, which connect bosons (integer-spin particles) with fermions (half-integer-spin particles), and for leptoquarks, which mix the fundamental quarks with leptons. Alternatively, indirect searches using precise measurements of well predicted standard-model observables allow highly targeted alternative tests for physics beyond the standard model because they can reach mass and energy scales beyond those directly accessible by today's high-energy accelerators. Such an indirect search aims to determine the weak charge of the proton, which defines the strength of the proton's interaction with other particles via the well known neutral electroweak force. Because parity symmetry (invariance under the spatial inversion $(x, y, z) \rightarrow (-x, -y, -z)$) is violated only in the weak interaction, it provides a tool with which to isolate the weak interaction and thus to measure the proton's weak charge¹. Here we report the value 0.0719 ± 0.0045 , where the uncertainty is one standard deviation, derived from our measured parity-violating asymmetry in the scattering of polarized electrons on protons, which is -226.5 ± 9.3 parts per billion (the uncertainty is one standard deviation). Our value for the proton's weak charge is in excellent agreement with the standard model² and sets multi-teraelectronvolt-scale constraints on any semi-leptonic parity-violating physics not described within the standard model. Our results show that precision parity-violating measurements enable searches for physics beyond the standard model that can compete with direct searches at high-energy accelerators and, together with astronomical observations, can provide fertile approaches to probing higher mass scales.

In the electroweak standard model, elastic scattering is mediated by the exchange of neutral currents (virtual photons and Z^0 bosons) between fundamental particles. A particle's weak charge, Q_w , is analogous to—but distinct from—its electric charge, q ; the former quantifies the vector coupling of the Z^0 boson to the particle, whereas the latter quantifies the vector coupling of the photon to the particle. The proton's weak charge Q_w^p is defined¹ as the sum of the weak vector coupling constants C_{1q} of the Z^0 boson to its constituent up (u) and down (d) quarks:

$$Q_w^p = -2(C_{1u} + C_{1d}) \quad (1)$$

The Z^0 exchange contribution to electron–proton scattering can be isolated via the weak interaction's unique parity-violation signature

(see Fig. 1). Interference between electromagnetic and weak scattering amplitudes leads to a parity-violation asymmetry A_{ep} that can be measured with a longitudinally polarized electron beam incident on an unpolarized-proton target:

$$A_{\text{ep}} = \frac{\sigma_+ - \sigma_-}{\sigma_+ + \sigma_-} \quad (2)$$

Here, σ_{\pm} represents the cross-section of the helicity-dependent elastic scattering (ep) of polarized electrons (e) on protons (p), integrated over the scattered-electron detector acceptance. Helicity (± 1) indicates the spin direction of the electrons in the beam as either parallel ($+1$) or anti-parallel (-1) to their momenta.

Measuring A_{ep} at a small four-momentum transfer (Q^2) suppresses contributions from the proton's extended structure relative to the proton's weak charge Q_w^p . However, A_{ep} is small at small Q^2 values, making its measurement challenging. In the low- Q^2 limit, the parity-violation asymmetry can be expressed¹ as:

$$A_{\text{ep}}/A_0 = Q_w^p + Q^2 B(Q^2, \theta) \quad (3)$$

where $A_0 = -G_F Q^2 / (4\pi\alpha\sqrt{2})$, $-Q^2$ is the four-momentum transfer squared, $B(Q^2, \theta)$ represents the proton's extended structure defined in terms of electromagnetic, strange and axial form factors, θ is the (polar) scattering angle of the electron in the laboratory frame with respect to the beam axis, G_F is the Fermi constant and α is the fine-structure constant.

The Q_{weak} experiment^{3,4} (see Extended Data Fig. 1) used a beam of longitudinally polarized electrons accelerated to 1.16 GeV at the Thomas Jefferson National Accelerator Facility. Three sequential acceptance-defining lead collimators, matched to an eight-sector azimuthally symmetric toroidal magnet, selected electrons scattered from a liquid-hydrogen target at angles between 5.8° and 11.6° . In each magnet octant, elastically scattered electrons were directed to a quartz detector fronted by lead pre-radiators. Cherenkov light produced by the electromagnetic shower passing through the quartz was converted to a current by photomultiplier tubes at each end of the quartz bars. These currents were integrated for each 1-ms-long helicity state of the beam. For calibration purposes, and to confirm our understanding of the acceptance and backgrounds, drift chambers were periodically inserted upstream and downstream of the magnet to track individual particles during dedicated periods of low-current running.

To achieve a precision of less than 10 parts per billion (p.p.b.), this experiment pushed existing boundaries on many fronts: higher polarized-beam intensity (180 μA), faster beam-helicity reversal (960 s^{-1}), better GeV-scale beam polarimetry⁵ precision ($\pm 0.6\%$), higher liquid-hydrogen target⁶ luminosity ($1.7 \times 10^{39} \text{ cm}^{-2} \text{ s}^{-1}$) and cooling power (3 kW) and higher total detection rates (7 GHz). Following a brief commissioning period, the experiment was divided into two roughly six-month run periods, between which improvements were made primarily to polarimetry and helicity-related beam-monitoring and control instrumentation. Further details, including the

*A list of participants and their affiliations appears at the end of this Letter.

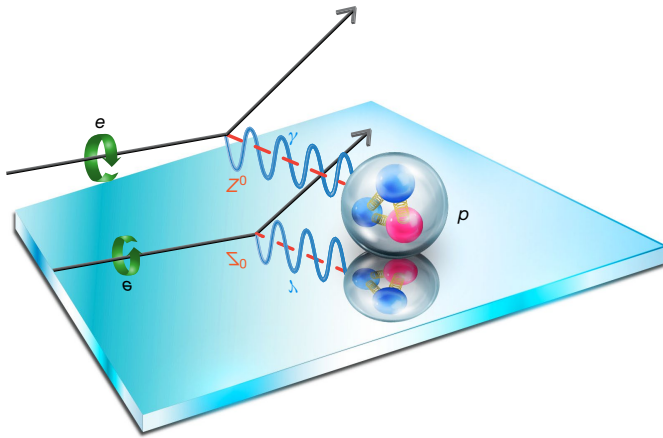


Fig. 1 | Parity-violating electron scattering from the proton. An incoming electron, e , with helicity $+1$ scatters away from the plane of the ‘parity-violating mirror’. The image in the parity-violating mirror shows the incoming electron with the opposite helicity, -1 ; instead of scattering into the plane of the parity-violating mirror (as it would in a real mirror), it scatters out of the plane of the parity-violating mirror. The dominant electromagnetic interaction, mediated by the photon (γ , blue wavy line), conserves parity. The weak interaction, mediated by the neutral Z^0 boson (dashed red line), violates parity. The weak interaction is studied experimentally by exploiting parity violation through reversals of the incident-beam helicity, which mimic the parity-violating mirror ‘reflection’.

backgrounds and corrections associated with each of the two halves of the experiment, are provided in Methods.

The asymmetry measurement results are $A_{ep} = -223.5 \pm 15.0$ (statistical) ± 10.1 (systematic) p.p.b. in the first half of the experiment, and $A_{ep} = -227.2 \pm 8.3$ (statistical) ± 5.6 (systematic) p.p.b. in the second half. These values are in excellent agreement with each other and consistent with our previously published commissioning result³. Accounting for correlations in some systematic uncertainties between the two measurement periods, the combined result is $A_{ep} = -226.5 \pm 7.3$ (statistical) ± 5.8 (systematic) p.p.b. The total uncertainty achieved (9.3 p.p.b.) sets a new level of precision for parity-violating electron scattering (PVES) from a nucleus.

The relationship between the measured asymmetries A_{ep} and the proton’s weak charge Q_w^p is expressed by equation (3), where the hadronic-structure-dependent term $B(Q^2, \theta)$ grows with the momentum transfer Q^2 . Higher- Q^2 data from previous PVES experiments (see online references, Methods) were included in a global fit^{3,7,8} to constrain the proton-structure contributions for the short extrapolation from our datum to $Q^2 = 0$ in order to determine Q_w^p , the intercept of equation (3). The average Q^2 of this experiment ($0.0248 \text{ GeV}^2 c^{-2}$) is much smaller than that of any other PVES experiments used in this fit, with correspondingly smaller contributions from the proton structure. The superior precision of the Q_{weak} measurement tightly constrains the fit near $Q^2 = 0$, where the connection to Q_w^p can be made.

The parameters of the global fit^{3,7,8} to the PVES data are the axial-electron–vector-quark weak-coupling constants C_{1u} and C_{1d} , the strange charge radius ρ_s and strange magnetic moment μ_s (which characterize the strength of the proton’s electric and magnetic strange-quark form factors) and the strength of the neutral weak (Z^0 exchange) isovector ($T = 1$) axial form factor $G_A^{Z(T=1)}$. The EM form factors G_E and G_M used in the fit were taken from ref. ⁹; uncertainties in this input were accounted for in the result for Q_w^p and in its uncertainty.

The ep asymmetries shown in Fig. 2 were corrected^{1,3} for the energy-dependent part of the γZ -box weak radiative correction^{10–13} and its uncertainty. No other electroweak radiative corrections need to be applied to determine Q_w^p . However, ordinary electromagnetic radiative corrections (bremsstrahlung) were accounted for in the asymmetries used in the fit, including our datum. Details of the fitting procedure, as

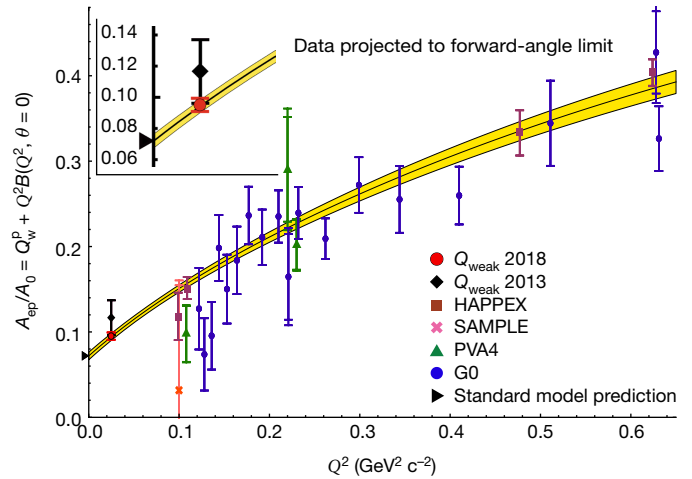


Fig. 2 | The reduced asymmetry $A_{ep}/A_0 = Q_w^p + Q^2 B(Q^2, \theta = 0)$ versus Q^2 . The global fit is illustrated using ep asymmetries from this experiment ($Q_{\text{weak}} 2018$), from the commissioning phase of this experiment³ ($Q_{\text{weak}} 2013$), as well as from the earlier experiments HAPPEX, SAMPLE, PVA4 and G0 (see Methods), projected to $\theta = 0^\circ$ and reduced by a factor $A_0(Q^2)$ appropriate for each datum. The data shown here include the γZ -box radiative correction and uncertainty. Inner error bars correspond to one standard deviation (s.d.) and include statistical and systematic uncertainties. Outer error bars on the data indicate the additional uncertainty estimated from the forward-angle projection (for some data points, inner and outer error bars coincide). The solid line represents the global fit to the complete PVES database (see Methods), and the yellow band indicates the fit uncertainty (1 s.d.). The arrowhead at $Q^2 = 0$ indicates the standard-model prediction², $Q_w^p = 0.0708(3)$, which agrees well with the intercept of the fit ($Q_w^p = 0.0719 \pm 0.0045$). The inset shows a magnification of the region around this experiment’s result, at $\langle Q^2 \rangle = 0.0248 \text{ GeV}^2 c^{-2}$.

well as a description of the corrections applied to the asymmetry for this experiment, are described in Methods.

The global fit is shown in Fig. 2 together with the ep data, expressed as $A_{ep}(Q^2, \theta = 0)/A_0$. To isolate the Q^2 dependence for this figure, the θ dimension was projected to 0° by subtracting [$A_{\text{calc}}(Q^2, \theta) - A_{\text{calc}}(Q^2, \theta = 0)$] from the measured asymmetries $A_{ep}(Q^2, \theta)$, as described in refs ^{3,8}. Here A_{calc} refers to the asymmetries determined from the global fit. The fit includes all relevant PVES data for the scattering of polarized electrons on protons (ep), deuterons ($e^2\text{H}$) and ^4He ($e^4\text{He}$); see Methods. The PVES database provides a data-driven (as opposed to a more theoretical) constraint on the nucleon structure uncertainties in the extrapolation to $Q^2 = 0$. We consider this to be the best method to provide our main result (denoted in Table 1 as

Table 1 | Results extracted from the asymmetry measured in the Q_{weak} experiment

Method	Quantity	Value	Error
PVES fit	Q_w^p	0.0719	0.0045
	ρ_s	0.20	0.11
	μ_s	-0.19	0.14
	$G_A^{Z(T=1)}$	-0.64	0.30
PVES fit + APV	Q_w^p	0.0718	0.0044
	Q_w^n	-0.9808	0.0063
	C_{1u}	-0.1874	0.0022
	C_{1d}	0.3389	0.0025
	C_1 correlation	-0.9318	
PVES fit + LQCD	Q_w^p	0.0685	0.0038
Q_{weak} datum only	Q_w^p	0.0706	0.0047
Standard model	Q_w^p	0.0708	0.0003

‘PVES fit’ refers to a global fit incorporating the Q_{weak} result and the PVES database, as described in Methods. When combined with APV^{14,15} (to improve the C_{1u} precision), this method is denoted as ‘PVES fit + APV’. If the strange form factors in the global fit (without APV) are constrained to match LQCD calculations¹⁶, we label the result as ‘PVES fit + LQCD’. The method labelled ‘ Q_{weak} datum only’ uses the Q_{weak} datum, together with electromagnetic⁹, strange¹⁶ and axial¹⁸ form factors from the literature in lieu of the global fit. Uncertainties are 1 s.d.

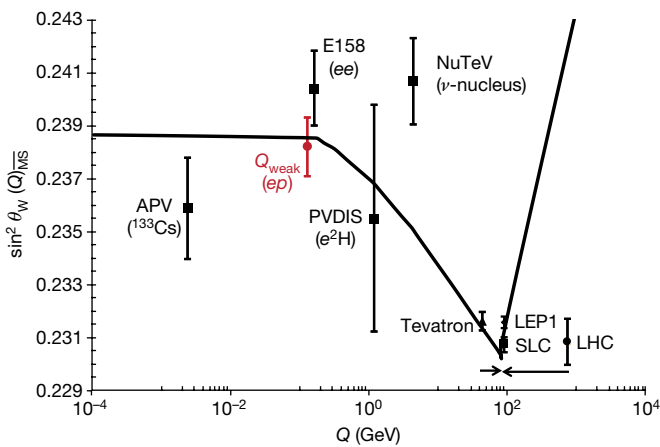


Fig. 3 | Variation of $\sin^2\theta_W$ with energy scale Q . The modified-minimal-subtraction (\overline{MS}) scheme is shown as the solid curve^{2,19}, together with experimental determinations at the Z^0 pole² (Tevatron, LEP1, SLC, LHC), from APV on caesium^{14,15}, Møller scattering (E158)²², deep inelastic scattering of polarized electrons on deuterons (e^2H ; PVDIS)²³ and from neutrino–nucleus scattering (NuTeV)²⁴. It has been argued²⁵, however, that the latter result contains substantial unaccounted-for nuclear physics effects, such as neutron-excess corrections to the quark momenta, charge-symmetry breaking and strange-quark momentum asymmetries. Our new result is plotted in red at the energy scale of the Q_{weak} experiment, $Q = 0.158$ GeV (slightly offset horizontally for clarity). Error bars (1 s.d.) include statistical and systematic uncertainties.

‘PVES fit’), which is $Q_W^p = 0.0719 \pm 0.0045$. Below we discuss the sensitivity of this result to variations in the experimental and theoretical input used to determine it.

Just as the proton’s weak charge depends on its u and d quark content (see equation (1)), the weak charge of other nuclear systems depends on their (different) u and d quark content. Because ep , e^2H and e^4He data are included in the global fit, C_{1u} and C_{1d} are reasonably well determined. However, if the very precise atomic-parity violation (APV) result^{14,15} on ^{133}Cs is also included in the global fit, C_{1u} and C_{1d} can be determined with greater precision and then used to extract the neutron’s weak charge $Q_W^n = -2(C_{1u} + 2C_{1d})$. We note that inclusion or exclusion of the APV result has negligible impact on our result for Q_W^p , which is derived from the intercept of the global fit. The results for C_{1u} , C_{1d} , Q_W^p and Q_W^n obtained by including APV in the PVES global fit, which are listed in Table 1 as ‘PVES fit + APV’, are in agreement with the standard-model values².

While our preferred result is based on the data-driven analysis of PVES fit, the final determination of the weak charge of the proton does not change appreciably with additional theoretical constraints. One of the dominant uncertainties in the term $B(Q^2, \theta)$ of equation (3) arises from the knowledge of the strange-quark contributions. These have been determined very precisely in recent theoretical calculations^{16,17} employing lattice quantum chromodynamics (LQCD). Using these theoretical results to constrain the extrapolation to $Q^2 = 0$ results in a slightly lower weak charge and a reduction in the uncertainty, as shown in Table 1 (‘PVES fit + LQCD’). The APV result was not included in this determination of Q_W^p ; its inclusion makes negligible difference.

Because the proximity to threshold ($Q^2 \rightarrow 0$) and precision of our Q_{weak} result overwhelmingly dominate the fits described above, it is possible to go one step further and use the Q_{weak} datum by itself to determine Q_W^p . The fact that the strange and axial form factors contribute so little at the kinematics of the Q_{weak} experiment (0.1% and 2.5%, respectively) also helps motivate this consistency check. Using the same electromagnetic form factors⁹ as in the fits above, the same lattice calculation¹⁶ for the strange form factors, and following the extraction method of ref. 18 for the axial form factor, the Q_W^p result obtained by using just the Q_{weak} datum falls in-between the consistent results of the

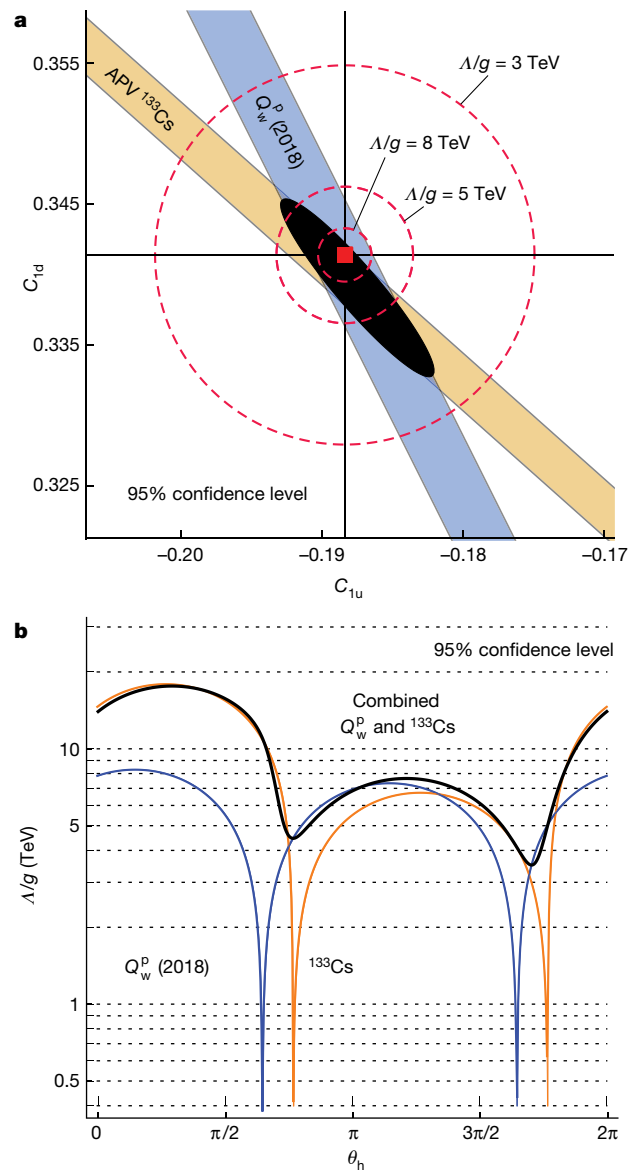


Fig. 4 | Mass and coupling constraints on new physics. **a**, Constraints, at the 95% confidence level, on the axial-electron–vector-quark weak-coupling constants C_{1u} and C_{1d} , derived from the weak charge determined in this experiment using the global fit method ‘PVES fit’ (blue band) and the APV result^{2,14,15} on ^{133}Cs (gold band). The combined (95% confidence level) constraint is shown by the black ellipse. Contours of the mass reach Λ/g for new physics with coupling g to arbitrary quark-flavour ratios are indicated by dashed circles centred about the standard-model values² of C_{1u} and C_{1d} , which are denoted by the red square. **b**, Mass reach Λ/g (95% confidence level) as a function of the quark-flavour mixing angle θ_h for the Q_{weak} ‘PVES fit’ result (blue curve), for the ^{133}Cs APV^{14,15} result² (gold curve) and for both results combined (black curve). The two maxima in the blue curve at $\theta_h = \tan^{-1}(n_d/n_u) = \tan^{-1}(1/2) = 26.6^\circ$ and 206.6° correspond to $\Lambda_-/g = 8.4$ TeV and $\Lambda_+/g = 7.4$ TeV in equation (4), respectively.

other determinations described above, which employ the entire PVES database (see Table 1, ‘ Q_{weak} datum only’). The uncertainty of the Q_W^p result in this case includes an additional uncertainty (4.6 p.p.b.) due to the calculated form factors, but is only 4% larger than the uncertainty of the global fit result, which uses the entire PVES database. The dominant correction, from the electromagnetic form factors (23.7%), is well known in the low- Q^2 regime of the Q_{weak} experiment.

The Q_W^p determinations described above can be used to test the prediction of the standard model for $\sin^2\theta_W$, the fundamental

electroweak parameter characterizing the mixing of the electromagnetic and weak interactions in the standard model (θ_W is the Weinberg angle). By neglecting small quantum corrections, the standard model derives^{19,20} $\sin^2\theta_W$ in terms of the electroweak boson masses, M_W and M_Z , as $\sin^2\theta_W = 1 - (M_W/M_Z)^2 \approx 1/4$, and so $Q_W^p = 1 - 4\sin^2\theta_W$ is nearly zero. This ‘accidental’ standard-model suppression of Q_W^p makes it an ideal observable in the search for new parity-violation interactions of natural size²¹. Using the latest input² to calculate quantum corrections that relate¹ $\sin^2\theta_W(Q=0)$ to Q_W^p , as described in Methods, we obtain $\sin^2\theta_W(Q=0)_{\overline{\text{MS}}} = 0.2383 \pm 0.0011$ in the modified-minimal-subtraction ($\overline{\text{MS}}$) scheme^{2,19}.

Figure 3 shows our $\sin^2\theta_W$ result (after subtracting 0.00012 to plot it at the Q_{weak} energy scale, 0.158 GeV), along with other $\sin^2\theta_W$ determinations^{2,20,22–25}. Our value is consistent with the standard-model expectation and the purely leptonic E158 result²² obtained in Møller (ee) scattering, which has different sensitivities to new physics from our semi-leptonic (ep) result. Although the measurements at the Z^0 pole are more precise than our result, there exist a variety of beyond-standard-model (BSM) scenarios that can have considerable influence on low-energy precision measurements but little effect on collider measurements at the Z^0 -mass energy scale²⁶. An example is the dark-photon model of ref. ²⁷, which allows large effects for dark Z mediators of a few hundred megaelectronvolts at low Q , but no effects at the Z^0 pole.

To explore this experiment’s sensitivity to new BSM contact interactions, we follow the convention²⁸ where a ‘new physics’ term, g^2/Λ^2 , is added to the standard-model term $g_{AV}^{\text{eq}}/(2\nu^2)$ used in the Lagrangian to describe the neutral-current interaction of axial-vector electrons with vector quarks. (This convention differs from an earlier one¹ by a factor of 4; a factor of 2 in Λ). Here $g_{AV}^{\text{eq}} = C_{1q} = 2g_A^e g_V^q$ is the standard-model axial-electron–vector-quark coupling, $\nu^2 = \sqrt{2}/(2G_F)$, and Λ represents the mass reach for new physics (the mass of the hypothetical BSM particle being exchanged) with coupling g . Expressed in terms of Q_W^p and its uncertainty, $\pm \Delta Q_W^p$, the 95%-confidence-level mass reach is

$$\frac{\Lambda_{\pm}}{g} = \nu \sqrt{\frac{4\sqrt{5}}{|Q_W^p \pm 1.96\Delta Q_W^p - Q_W^p(\text{SM})|}} \quad (4)$$

where $\Lambda_+/g = 7.4$ TeV and $\Lambda_-/g = 8.4$ TeV.

For the extreme contact-interaction coupling²⁹ $g^2 = 4\pi$, the maximum mass reach for new semi-leptonic physics determined by our Q_W^p result is $\Lambda_+ = 26.3$ TeV. Using the coupling $g^2 = 4\pi\alpha$, which is typically assumed for leptoquarks³⁰ (hypothetical BSM particles with both lepton and baryon numbers; see also <http://pdglive.lbl.gov/DataBlock.action?node=S056ESP&init=0>), equation (4) rules out leptoquark masses below 2.3 TeV.

In a more general case⁸ where the coupling of the new physics to the quarks is not restricted to the same 2:1 ratio of u to d quarks as in the proton, the mass reach can be expressed as a circle of radius $(g/\Lambda)^2 \sqrt{2}/G_F$, about the standard-model origin $(C_{1u}^{\text{SM}}, C_{1d}^{\text{SM}}) = (-0.1887, 0.3419)$ in C_{1q} space. This is illustrated in Fig. 4a, which also shows the complementary constraints on C_{1q} provided by the weak-charge measurements of this experiment ($Q_W^p = -2(2C_{1u} + C_{1d})$) and the ¹³³Cs APV^{14,15} result² ($Q_W^{\text{Cs}} = -2[55(2C_{1u} + C_{1d}) + 78(C_{1u} + 2C_{1d})]$). The isospin dependence of potential BSM physics can be expressed in terms of the projections $h_v^u = \cos\theta_h$ and $h_v^d = \sin\theta_h$, where θ_h is the quark-flavour mixing angle, the superscripts u and d refer to the quark flavour and the subscript refers to the vector piece, as in ref. ⁸. We then obtain the 95%-confidence-level bounds from this experiment, which are shown in Fig. 4b, together with those from APV^{2,14,15} and from combining those two constraints. New physics is ruled out below the curves. Our combined constraint raises the θ_h -independent limit for generic new semi-leptonic parity-violation BSM physics to 3.5 TeV.

The low-energy precision frontier continues to offer an exciting landscape to search for BSM physics. The results of this experiment are

consistent with the standard model and place important limits on new beyond-standard-model physics. Future experiments propose to provide even more precise (and much more challenging) determinations of Q_W^p at lower Q^2 (ref. ³¹) and of Q_W^e (ref. ³²) by taking the techniques and lessons learned in this experiment to the next level.

Online content

Any Methods, including any statements of data availability and Nature Research reporting summaries, along with any additional references and Source Data files, are available in the online version of the paper at <https://doi.org/10.1038/s41586-018-0096-0>.

Received: 12 October 2017; Accepted: 5 April 2018;

Published online 9 May 2018.

1. Erler, J., Kurylov, A. & Ramsey-Musolf, M. J. Weak charge of the proton and new physics. *Phys. Rev. D* **68**, 016006 (2003).
2. Particle Data Group. Review of particle physics. *Chinese Phys. C* **40**, 100001 (2016).
3. Androić, D. et al. First determination of the weak charge of the proton. *Phys. Rev. Lett.* **111**, 141803 (2013).
4. Allison, T. et al. The Q_{weak} experimental apparatus. *Nucl. Instrum. Meth. A* **781**, 105–133 (2015).
5. Narayan, A. et al. Precision electron-beam polarimetry at 1 GeV using diamond microstrip detectors. *Phys. Rev. X* **6**, 011013 (2016).
6. Smith, G. R. The Q_{weak} target performance. *Nuovo Cim. C* **35**, 159–163 (2012).
7. Young, R. D., Roche, J., Carlini, R. D. & Thomas, A. W. Extracting nucleon strange and anapole form factors from world data. *Phys. Rev. Lett.* **97**, 102002 (2006).
8. Young, R. D., Carlini, R. D., Thomas, A. W. & Roche, J. Testing the standard model by precision measurement of the weak charges of quarks. *Phys. Rev. Lett.* **99**, 122003 (2007).
9. Arrington, J. & Sick, I. Precise determination of low- Q nucleon electromagnetic form factors and their impact on parity-violating e - p elastic scattering. *Phys. Rev. C* **76**, 035201 (2007).
10. Hall, N. L., Blunden, P. G., Melnitchouk, W., Thomas, A. W. & Young, R. D. Quark-hadron duality constraints on γZ box corrections to parity-violating elastic scattering. *Phys. Lett. B* **753**, 221–226 (2016).
11. Blunden, P. G., Melnitchouk, W. & Thomas, A. W. New formulation of γZ box corrections to the weak charge of the proton. *Phys. Rev. Lett.* **107**, 081801 (2011).
12. Blunden, P. G., Melnitchouk, W. & Thomas, A. W. γZ box corrections to weak charges of heavy nuclei in atomic parity violation. *Phys. Rev. Lett.* **109**, 262301 (2012).
13. Gorchtein, M., Horowitz, C. J. & Ramsey-Musolf, M. J. Model dependence of the γZ dispersion correction to the parity-violating asymmetry in elastic ep scattering. *Phys. Rev. C* **84**, 015502 (2011).
14. Wood, C. S. et al. Measurement of parity nonconservation and an anapole moment in cesium. *Science* **275**, 1759–1763 (1997).
15. Dzuba, V. A., Berengut, J. C., Flambaum, V. V. & Roberts, B. Revisiting parity nonconservation in cesium. *Phys. Rev. Lett.* **109**, 203003 (2012).
16. Green, J. et al. High-precision calculation of the strange nucleon electromagnetic form factors. *Phys. Rev. D* **92**, 031501 (2015).
17. Sufian, R. S. et al. Strange quark magnetic moment of the nucleon at the physical point. *Phys. Rev. Lett.* **118**, 042001 (2017).
18. Liu, J., McKeown, R. D. & Ramsey-Musolf, M. J. Global analysis of nucleon strange form factors at low Q^2 . *Phys. Rev. C* **76**, 025202 (2007).
19. Erler, J. & Ramsey-Musolf, M. J. Weak mixing angle at low energies. *Phys. Rev. D* **72**, 073003 (2005).
20. Kumar, K. S., Mantry, S., Marciano, W. J. & Souder, P. A. Low-energy measurements of the weak mixing angle. *Annu. Rev. Nucl. Part. Sci.* **63**, 237–267 (2013).
21. Seiberg, N. Naturalness versus supersymmetric non-renormalization theorems. *Phys. Lett. B* **318**, 469–475 (1993).
22. Anthony, P. L. et al. Precision measurement of the weak mixing angle in Møller scattering. *Phys. Rev. Lett.* **95**, 081601 (2005).
23. The Jefferson Lab PVDIS Collaboration. Measurement of parity violation in electron-quark scattering. *Nature* **506**, 67–70 (2014).
24. The NuTeV Collaboration. Precise determination of electroweak parameters in neutrino–nucleon scattering. *Phys. Rev. Lett.* **88**, 091802 (2002); erratum 90, 239902 (2003).
25. Bentz, W., Cloët, I. C., Londergan, J. T. & Thomas, A. W. Reassessment of the NuTeV determination of the weak mixing angle. *Phys. Lett. B* **693**, 462–466 (2010).
26. Erler, J. & Su, S. The weak neutral current. *Prog. Part. Nucl. Phys.* **71**, 119–149 (2013).
27. Davoudiasl, H., Lee, H.-S. & Marciano, W. J. Muon $g-2$, rare kaon decays, and parity violation from dark bosons. *Phys. Rev. D* **89**, 095006 (2014).

28. Erler, J., Horowitz, C. J., Mantry, S. & Souder, P. A. Weak polarized electron scattering. *Annu. Rev. Nucl. Part. Sci.* **64**, 269–298 (2014).
29. Eichten, E., Lane, K. D. & Peskin, M. E. New tests for quark and lepton substructure. *Phys. Rev. Lett.* **50**, 811–814 (1983).
30. Abramowicz, H. et al. Search for first-generation leptoquarks at HERA. *Phys. Rev. D* **86**, 012005 (2012).
31. Berger, N. et al. Measuring the weak mixing angle with the P2 experiment at MESA. *J. China Univ. Sci. Tech.* **46**, 481–487 (2016).
32. Benesch, J. et al. The MOLLER experiment: an ultra-precise measurement of the weak mixing angle using Møller scattering. Preprint at <https://arxiv.org/abs/1411.4088v2> (2014).

Acknowledgements This work was supported by the US Department of Energy (DOE) Contract number DEAC05-06OR23177, under which Jefferson Science Associates, LLC, operates the Thomas Jefferson National Accelerator Facility. Construction and operating funding for the experiment was provided through the US DOE, the Natural Sciences and Engineering Research Council of Canada (NSERC), the Canadian Foundation for Innovation (CFI), and the National Science Foundation (NSF) with university matching contributions from the College of William and Mary, Virginia Tech, George Washington University and Louisiana Tech University. We thank the staff of Jefferson Laboratory, in particular the accelerator operations staff, the target and cryogenic groups, the radiation control staff, as well as the Hall C technical staff for their help and support. We are grateful for the contributions of our undergraduate students. We thank TRIUMF for its contributions to the development of the spectrometer and integrated electronics, and BATES for its contributions to the spectrometer and Compton polarimeter. We are indebted to P. G. Blunden, J. D. Bowman, J. Erler, N. L. Hall, W. Melnitchouk, M. J. Ramsey-Musolf and A. W. Thomas for discussions. We also thank P. A. Souder for contributions to the analysis. Figure 2 was adapted with permission from ref. ³ (copyrighted by the American Physical Society).

Author contributions Authors contributed to one or more of the following areas: proposing, leading and running the experiment; design, construction, optimization and testing of the experimental apparatus and data acquisition system; data analysis; simulation; extraction of the physics results from measured asymmetries; and the writing of this Letter.

Competing interests The authors declare no competing interests.

Additional information

Extended data is available for this paper at <https://doi.org/10.1038/s41586-018-0096-0>.

Reprints and permissions information is available at <http://www.nature.com/reprints>.

Correspondence and requests for materials should be addressed to G.R.S.

Publisher's note: Springer Nature remains neutral with regard to jurisdictional claims in published maps and institutional affiliations.

The Jefferson Lab Q_{weak} Collaboration

D. Androić¹, D. S. Armstrong², A. Asaturyan³, T. Averett², J. Balewski⁴, K. Bartlett², J. Beaufait⁵, R. S. Beminiwattha⁶, J. Benesch⁵, F. Benmokhtar⁷, J. Birchall⁸, R. D. Carlini^{2,5*}, J. C. Cornejo², S. Covrig Dusa⁵, M. M. Dalton⁹, C. A. Davis¹⁰, W. Deconinck², J. Diefenbach¹¹, J. F. Dowd², J. A. Dunne¹², D. Dutta¹², W. S. Duval¹³, M. Elaasar¹⁴, W. R. Falk^{8,25}, J. M. Finn^{2,26}, T. Forest^{15,16}, C. Gai⁹, D. Gaskell⁵, M. T. W. Gericke⁸, J. Grames¹⁷, V. M. Gray², K. Grimm^{2,16}, F. Guo⁴, J. R. Hoskins², D. Jones⁹, M. Jones⁵, R. Jones¹⁸, M. Kargiantoulakis⁹, P. M. King⁶, E. Korkmaz¹⁹, S. Kowalski⁴, J. Leacock¹³, J. Leckey², A. R. Lee¹³, J. H. Lee^{2,6}, L. Lee^{8,10}, S. MacEwan⁸, D. Mack⁵, J. A. Magee², R. Mahurin⁸, J. Mammei¹³, J. W. Martin²⁰, M. J. McHugh²¹, D. Meekins⁵, J. Mei⁵, K. E. Mesick²¹, R. Michaels⁵, A. Micherdzinska²¹, A. Mkrtchyan³, H. Mkrtchyan³, N. Morgan¹³, A. Narayan¹², L. Z. Ndikum¹², V. Nelyubin⁹, H. Nuhait¹⁶, Nuruzzaman^{11,12}, W. T. H. van Oers^{8,10}, A. K. Opper²¹, S. A. Page⁸, J. Pan⁸, K. D. Paschke⁹, S. K. Phillips²², M. L. Pitt¹³, M. Poelker¹⁷, J. F. Rajotte⁴, W. D. Ramsay^{8,10}, J. Roche⁶, B. Sawatzky⁵, T. Seva¹, M. H. Shabestari¹², R. Silwal⁹, N. Simicevic¹⁶, G. R. Smith^{5*}, P. Solvignon^{5,26}, D. T. Spayde²³, A. Subedi¹², R. Subedi²¹, R. Suleiman¹⁷, V. Tadevosyan³, W. A. Tobias⁹, V. Tvaskis^{8,20}, B. Waidyawansa⁶, P. Wang⁸, S. P. Wells¹⁶, S. A. Wood⁵, S. Yang², R. D. Young²⁴, P. Zang²⁵ & S. Zhamkochyan³

¹Department of Physics, University of Zagreb, Zagreb, Croatia. ²Department of Physics, College of William and Mary, Williamsburg, VA, USA. ³Division of Experimental Physics, A. I. Alikhanyan National Science Laboratory (Yerevan Physics Institute), Yerevan, Armenia. ⁴Department of Physics, Massachusetts Institute of Technology, Cambridge, MA, USA. ⁵Physics Division, Thomas Jefferson National Accelerator Facility, Newport News, VA, USA. ⁶Department of Physics and Astronomy, Ohio University, Athens, OH, USA. ⁷Department of Physics, Christopher Newport University, Newport News, VA, USA. ⁸Department of Physics and Astronomy, University of Manitoba, Winnipeg, Manitoba, Canada. ⁹Department of Physics, University of Virginia, Charlottesville, VA, USA. ¹⁰Science Division, TRIUMF, Vancouver, British Columbia, Canada. ¹¹Department of Physics, Hampton University, Hampton, VA, USA. ¹²Department of Physics and Astronomy, Mississippi State University, Mississippi State, MS, USA. ¹³Department of Physics, Virginia Polytechnic Institute and State University, Blacksburg, VA, USA. ¹⁴Department of Natural Sciences, Southern University at New Orleans, New Orleans, LA, USA. ¹⁵Department of Physics, Idaho State University, Pocatello, ID, USA. ¹⁶Department of Physics, Louisiana Tech University, Ruston, LA, USA. ¹⁷Accelerator Division, Thomas Jefferson National Accelerator Facility, Newport News, VA, USA. ¹⁸Department of Physics, University of Connecticut, Storrs-Mansfield, CT, USA. ¹⁹Department of Physics, University of Northern British Columbia, Prince George, British Columbia, Canada. ²⁰Department of Physics, University of Winnipeg, Winnipeg, Manitoba, Canada. ²¹Department of Physics, George Washington University, Washington DC, USA. ²²Department of Physics, University of New Hampshire, Durham, NH, USA. ²³Physics Department, Hendrix College, Conway, AR, USA. ²⁴Department of Physics and Mathematical Physics, University of Adelaide, Adelaide, South Australia, Australia. ²⁵Department of Physics, Syracuse University, Syracuse, NY, USA. ²⁶Deceased: W. R. Falk, J. M. Finn, P. Solvignon. *e-mail: carlini@jlab.org; smithg@jlab.org

METHODS

Here we describe the formalism connecting the experimentally measured asymmetry A_{ep} to the proton's weak charge Q_{w}^{p} , the experimental method used to determine A_{ep} , some measures of the data quality, and the electroweak radiative corrections needed to extract the weak mixing angle from Q_{w}^{p} .

Formalism. The Q_{weak} experiment measured the parity-violating asymmetry A_{ep} , which is the normalized difference between the elastic-scattering cross-sections (σ) of longitudinally polarized electrons with positive (σ_{+}) and negative (σ_{-}) helicity from unpolarized protons:

$$A_{\text{ep}} = \frac{\sigma_{+} - \sigma_{-}}{\sigma_{+} + \sigma_{-}} \quad (5)$$

The extended structure of the proton can be represented using form factors. Assuming charge symmetry, the single-boson exchange ('tree-level') expression for the asymmetry can be written in terms of the proton and neutron electromagnetic form factors G_{E}^{p} , G_{M}^{p} , G_{E}^{n} and G_{M}^{n} , the strange electric and magnetic form factors G_{E}^{s} and G_{M}^{s} , and the neutral weak axial form factor G_{A}^{p} as^{7,33}

$$A_{\text{ep}} = A_0 \frac{A_{\text{v}}^{\text{p}} + A_{\text{s}}^{\text{p}} + A_{\text{a}}^{\text{p}}}{\varepsilon (G_{\text{E}}^{\text{p}})^2 + \tau (G_{\text{M}}^{\text{p}})^2} \quad (6)$$

with

$$\begin{aligned} A_0 &= \frac{-G_{\text{F}} Q^2}{4\pi\alpha\sqrt{2}} \\ A_{\text{v}}^{\text{p}} &= Q_{\text{w}}^{\text{p}} [\varepsilon (G_{\text{E}}^{\text{p}})^2 + \tau (G_{\text{M}}^{\text{p}})^2] \\ &\quad - [\varepsilon G_{\text{E}}^{\text{p}} G_{\text{E}}^{\text{n}} + \tau G_{\text{M}}^{\text{p}} G_{\text{M}}^{\text{n}}] \\ A_{\text{s}}^{\text{p}} &= -\varepsilon G_{\text{E}}^{\text{p}} G_{\text{E}}^{\text{s}} - \tau G_{\text{M}}^{\text{p}} G_{\text{M}}^{\text{s}} \\ A_{\text{a}}^{\text{p}} &= -(1 - 4\sin^2\theta_{\text{W}}) \varepsilon' G_{\text{M}}^{\text{p}} G_{\text{A}}^{\text{p}} \\ Q_{\text{w}}^{\text{p}} &= -2(2C_{1\text{u}} + C_{1\text{d}}) \end{aligned}$$

where the subscripts v, s and a refer to the vector, strange and axial contributions to the asymmetry, respectively,

$$\varepsilon = \frac{1}{1 + 2(1 + \tau)\tan^2(\theta/2)} \quad \text{and} \quad \varepsilon' = \sqrt{\tau(1 + \tau)(1 - \varepsilon^2)}$$

are kinematic quantities and $\tau = Q^2/(4M^2)$, where M is the proton mass.

By taking the limits $\theta \rightarrow 0$ and $Q^2 \rightarrow 0$, equation (6) is reduced³⁴ to equation (3). Although similar relationships apply for parity-violating elastic scattering from ^4He and quasi-elastic scattering from ^2H , these involve different linear combinations of $C_{1\text{u}}$ and $C_{1\text{d}}$ and the various form factors^{33,35}.

Global fit. Using equation (6), a global fit was made to a database that included all relevant PVES data up to $Q^2 = 0.63 \text{ GeV}^2 c^{-2}$: 28 electron-proton scattering results obtained by the G0^{36,37}, HAPPEX³⁸⁻⁴¹, SAMPLE⁴², PVA4⁴³⁻⁴⁵ and Q_{weak} ³ collaborations, including the present result, two ^4He elastic scattering results (HAPPEX^{40,46}) and five ^2H quasi-elastic scattering results (G0³⁷, PVA4^{45,47} and SAMPLE⁴⁸).

For the fit, we followed the procedure introduced by Young et al.⁷, as used in refs^{3,8}. We used six parameters in the fit; namely, $C_{1\text{u}}$, $C_{1\text{d}}$ and four parameters that characterize the strange and axial form factors: the strange radius ρ_{s} , the strange magnetic moment μ_{s} and the magnitudes of G_{A}^{p} and G_{A}^{n} . The parameterizations chosen for the strange form factors were $G_{\text{E}}^{\text{s}} = \rho_{\text{s}} Q^2 G_{\text{d}}$ and $G_{\text{M}}^{\text{s}} = \mu_{\text{s}} G_{\text{d}}$, with the dipole form factor $G_{\text{d}} = (1 - Q^2/\lambda^2)^{-2}$, where $\lambda = 1 \text{ GeV} c^{-1}$. Young et al.⁷ examined the consequences of using more elaborate Q^2 dependences for G_{E}^{s} and G_{M}^{s} and found that they were not required for the data. More recent analyses have come to the same conclusion^{18,49}. LQCD calculations^{16,17} have also found similar shapes for G_{E}^{s} and G_{M}^{s} . The neutron's axial form factor G_{A}^{n} enters the fit through the inclusion of ^2H data in the database. For the isovector combination $G_{\text{A}}^{Z(T=1)} = (G_{\text{A}}^{\text{p}} - G_{\text{A}}^{\text{n}})/2$, the dipole form G_{d} was again adopted, with the normalization factor as the parameter. Because the isoscalar combination $G_{\text{A}}^{Z(T=0)} = (G_{\text{A}}^{\text{p}} + G_{\text{A}}^{\text{n}})/2$ is known from the theory to be small, it was constrained in the fit to the theoretical value⁵⁰ $G_{\text{A}}^{Z(T=0)} = -0.08 \pm 0.26$, reducing the effective number of parameters to five. The unconstrained isovector combination $G_{\text{A}}^{Z(T=1)}$ presented in Table 1 was constructed from the values of G_{A}^{p} and G_{A}^{n} determined in the fit, which were $G_{\text{A}}^{\text{p}} = -0.59 \pm 0.34$ and $G_{\text{A}}^{\text{n}} = 0.68 \pm 0.44$ with a covariance of -0.0265 .

The electromagnetic form factors G_{E}^{p} , G_{M}^{p} , G_{E}^{n} and G_{M}^{n} were taken from ref.⁹. If, instead, we use any one of the several alternative parameterizations for these form factors⁵¹⁻⁵³, the fitted result for Q_{w}^{p} changes by less than 1%. We have incorporated this range as a systematic uncertainty.

Each of the experimental asymmetries A_{ep} used in the fit needed to be corrected for the one electroweak radiative correction with considerable energy dependence, the γZ -box diagram¹. Three independent theoretical groups have calculated this

correction, with results in excellent mutual agreement^{10,13,54}. We have adopted the most recent, which was obtained from a data-driven calculation of the vector¹⁰ (0.0054(4)) and axial-vector^{11,12} ($-0.0007(2)$) contributions, multiplied by a small Q^2 correction¹³ (0.978(12)); the numerical values given here are in terms of the effect on the reduced asymmetry A_{ep}/A_0 . The total correction to our datum is 0.0046(5), corresponding to a $6.4\% \pm 0.6\%$ correction to Q_{w}^{p} . If, instead, we use the calculations of either ref.¹³ or ref.⁵⁴, the extracted value of Q_{w}^{p} is essentially unchanged, and the effect on its uncertainty is negligible.

The fit was done using linear χ^2 minimization, with a resulting $\chi^2/\text{d.o.f.} = 1.25$ for 29 degrees of freedom (d.o.f.).

Apparatus. The Q_{weak} experiment was performed using a custom apparatus installed in Hall C at the Thomas Jefferson National Accelerator Facility. A complete description of the apparatus and critical aspects of the accelerator can be found in ref.⁴. Here we highlight some of the most important details illustrated in Extended Data Fig. 1.

The electron beam was longitudinally polarized and its helicity was reversed at a rate of 960 Hz in a pseudorandom sequence of 'helicity quartets' ($+-+ -$) or ($-++ -$). The quartet pattern minimized noise due to slow linear drifts, and the rapid helicity reversal limited noise due to fluctuations in the target density and beam properties. As a test for possible false asymmetries, two methods were used to reverse the beam helicity on a slower timescale than the rapid helicity reversal. About every 8 h, the helicity of the laser beam that was used to generate the polarized electron beam was reversed by insertion of a half-wave plate in its path. The helicity of the electron beam in the accelerator's injector region was reversed monthly using a 'double Wien' spin rotator⁵⁵. Non-vanishing correlations between the properties of the electron beam (intensity, position, angle and energy) and its helicity lead to false contributions to the measured asymmetry. These helicity-correlated beam properties were suppressed by carefully setting up the helicity-defining optics and active-feedback systems in the polarized injector laser system. The electron beam transport line was instrumented to allow the correction of residual helicity-correlated beam properties. Beam monitors upstream of the experimental apparatus provided continuous, non-invasive measurement of the electron beam's intensity, position, angle and energy. The response of the experimental apparatus to changes in the beam properties was periodically measured using a beam modulation system that generated controlled variations in the beam's position and angle using magnets and in its energy using a radio-frequency accelerating cavity. Finally, the electron beam's polarization was measured with two independent polarimeters upstream of the Q_{weak} apparatus.

The experiment usually ran with a 180- μA beam of 1.16-GeV, $\sim 88\%$ longitudinally polarized electrons incident on a 34.4-cm-long liquid hydrogen target placed in an aluminium cell and maintained at 20 K. A set of three lead collimators restricted the polar scattering angle acceptance to the range $5.8^\circ \leq \theta \leq 11.6^\circ$ with an azimuthal angle coverage of 49% of 2π . A resistive toroidal magnet between the target and detectors separated the elastically scattered electrons of interest from irreducible backgrounds arising from inelastic and Møller scattering. The resulting scattered electrons were detected in eight synthetic-quartz Cherenkov detectors, each 200 cm \times 18 cm \times 1.25 cm, arranged in an azimuthally symmetric pattern about the beam axis. Fourfold azimuthal symmetry was important to minimize and characterize the effects of helicity-correlated beam properties and residual transverse beam polarization. These 'main' detectors were equipped with 2-cm-thick Pb pre-radiators that amplified the electron signal and suppressed low-energy backgrounds. Light was collected from the detectors by photomultiplier tubes (PMTs) at each end. The high rates of ~ 800 MHz per detector required a current-mode readout, in which the PMT anode current was converted to a voltage that was digitized and integrated about every millisecond. Photographs of the apparatus are shown in Extended Data Fig. 1.

The collimator-magnet configuration and carefully designed shielding were effective in minimizing reducible sources of background, such as direct line-of-sight (neutral) tracks originating in the target and secondary scattering from the beam pipe. The residual diffuse background was monitored by background detectors in the main-detector shield house. These consisted of a complete main detector placed in the super-elastic region, a dark box with a bare PMT and a dark box with a PMT attached to a light guide. A symmetric array of four smaller detectors ('upstream luminosity monitors') placed on the upstream face of the defining (middle) collimator was effective in monitoring residual backgrounds from the tungsten beam collimator that shielded the downstream region from small-angle-scattered particles.

Finally, a tracking system consisting of drift chambers located before and after the magnet was deployed periodically to verify the acceptance-weighted kinematic distribution and to help study the backgrounds. These measurements were done in special run periods at very low beam currents (0.1–200 nA) and using conventional individual pulse counting.

Data from the experiment's short commissioning run (4% of the size of the dataset reported here) have been previously published³. Here we report the combined result from two run periods (referred to as Run 1 and Run 2), each about six months in duration. Because improvements were made to the apparatus between the two run periods and their beam conditions were different, we report the corrections and systematic uncertainties for each run period separately. To prevent possible biases in the analysis, the main-detector asymmetries were blinded by an additive shift in the asymmetry that was different for each run period. When the data analysis was complete, the asymmetries were unblinded, revealing the results presented here.

Data analysis. The raw asymmetry A_{raw} was formed from the normalized cross-section difference of equation (5) over the sum of the beam-charge normalized detector PMT signals, summed over the 8 detectors. The measured asymmetry A_{msr} was calculated from A_{raw} by correcting for a variety of effects that could cause false asymmetries:

$$A_{\text{msr}} = A_{\text{raw}} + A_t + A_l + A_{\text{bcm}} + A_{\text{bb}} + A_{\text{beam}} + A_{\text{bias}} \quad (7)$$

The methods for determining each of these corrections and their uncertainties are discussed below.

Transverse asymmetry correction, A_t . A small ($\sim 2\%$) residual transverse component of the incident beam polarization resulted in a transverse asymmetry A_t , which is driven by a parity-conserving two-photon-exchange amplitude⁵⁶. To determine this correction, we measured the transverse asymmetry using a maximally transversely polarized incident beam⁵⁷, which we used to calculate an upper bound on the broken symmetry of the spectrometer-detector system ($< 1.3\%$). By combining these effects with the measured residual transverse polarization components of the beam during data-taking with a nominally longitudinally polarized beam, we determined the correction to be $A_t = 0.0 \pm 1.1$ p.p.b. and $A_t = 0.0 \pm 0.7$ p.p.b. for Run 1 and Run 2, respectively.

Linearity correction, A_l . The nonlinearity of the Cherenkov detector readout chain (PMT, low-noise voltage-to-current preamplifier and analogue-to-digital converter) was directly measured using a system with light-emitting diodes and was found to be $0.7\% \pm 0.5\%$ at signal levels corresponding to those recorded during the experiment. This results in an additive correction $A_l = 1.3 \pm 1.0$ p.p.b. and $A_l = 1.2 \pm 0.9$ p.p.b. for Run 1 and Run 2, respectively.

Beam current monitor correction, A_{bcm} . The beam current was measured non-invasively with radio-frequency resonant cavities to allow a precise relative comparison of the beam charge in each helicity state. Two such beam current monitors (BCMs) were used in Run 1, while three BCMs were used in Run 2 after the installation of an additional monitor and improvement of the low-noise digital demodulation electronics. The correction A_{bcm} is zero by definition because in each period we normalize the integrated detector signals to the average of the BCM signals. The systematic uncertainty on this correction is determined from the variation in the reported charge asymmetry for the BCMs in each analysis, resulting in $\delta A_{\text{bcm}} = \pm 4.4$ p.p.b. and $\delta A_{\text{bcm}} = \pm 2.1$ p.p.b. for Run 1 and Run 2, respectively.

Beamline background asymmetry correction, A_{bb} . False asymmetry caused by secondary events scattered from the beamline and the tungsten beam collimator is referred to as the beamline background asymmetry A_{bb} . Such events were determined to be predominantly due to low-energy neutral particles and contributed a small amount to the signal (0.19%) but had a large asymmetry, which is believed to be associated with a helicity-dependent intensity or position variation in the extended halo around the main accelerated beam. Although their contribution was only a small component of the main detector signal, it dominated the asymmetry measurement of the background detectors, which were highly correlated (see Extended Data Fig. 2b). A direct correlation between the main-detector asymmetry from these events and the background asymmetries measured by the background detectors was shown by blocking two of the eight openings in the first of the three Pb collimators with 5.1-cm-thick tungsten plates (see Extended Data Fig. 2a). To correct for this false asymmetry, a correlation factor was extracted (separately for Run 1 and Run 2) between the asymmetries of the main detector array and the upstream luminosity monitor array, as shown in Extended Data Fig. 2c. The correlation factor was combined with the measured upstream luminosity monitor asymmetry, averaged every 6 min, to correct the main-detector asymmetry in that interval. The resulting net corrections for Run 1 and Run 2 were $A_{\text{bb}} = 3.9 \pm 4.5$ p.p.b. and $A_{\text{bb}} = -2.4 \pm 1.1$ p.p.b., respectively, where the uncertainty includes contributions from the statistical error on the determination of the correlation, as well as systematic errors extracted by allowing the correlation factor to vary randomly within a reasonable range over different time periods⁵⁸.

Correction for helicity-correlated beam properties, A_{beam} . Residual non-vanishing correlations in the properties of the electron beam were accounted for through the correction A_{beam} . Five beam properties—the transverse beam position and angle (horizontal X, X' ; vertical Y, Y'), as well as the energy—were monitored continuously as described above. The run-averaged helicity-correlated values of these

parameters are presented in Extended Data Table 1. Using the measured helicity-correlated beam differences $\Delta\chi_i$ and the sensitivity of the measured asymmetry to variations in the beam parameters $\partial A/\partial\chi_i$, the corrections for the i th beam parameter were combined into the total correction:

$$A_{\text{beam}} = - \sum_{i=1}^5 \left(\frac{\partial A}{\partial\chi_i} \right) \Delta\chi_i$$

The detector sensitivities $\partial A/\partial\chi_i$ were measured routinely by varying the beam parameters using the beam modulation system described above. This system created small perturbations of the beam parameters about their nominal values with a sinusoidal driving function at 125 Hz. Furthermore, an accelerator fast-feedback system with an operational frequency range that included 125 Hz was used, driving the beam position and angle parameters with a sinusoidal pattern that was 90° out of phase with respect to the beam modulation system. The result was that the beam parameters were driven in more than one way, allowing for redundant measurements of the detector sensitivities using different combinations of the driven signals. The spread in those results was the dominant component of the systematic uncertainty for this correction. Typical values of the sensitivities are shown in Extended Data Table 1. For a perfectly symmetric apparatus, the position and angle sensitivities would be zero. For this apparatus, the sensitivities show that the horizontal plane had a larger broken symmetry than the vertical plane. The resulting corrections were $A_{\text{beam}} = 18.5 \pm 4.1$ p.p.b. and $A_{\text{beam}} = 0.0 \pm 1.1$ p.p.b. for Runs 1 and 2, respectively. The considerably smaller correction in Run 2 was due to smaller position and angle helicity-correlated differences during that period.

Rescattering bias, A_{bias} . When comparing the measured asymmetry in the two PMTs ('left' and 'right') that read out the signal at each end of the eight main detectors, we found a consistent difference of about ± 300 p.p.b., as shown in Extended Fig. 3a. Here, 'right' is the beam direction \hat{k} crossed with the radial direction $\hat{r}, \hat{k} \times \hat{r}$. This effect is due to the left/right analysing power of the multiple scattering of transversely (radially) polarized electrons through the Pb pre-radiators of the main detectors. For perfect symmetry, this parity-conserving effect cancels when forming the parity-violating asymmetry of interest. Properly accounting for the minor broken symmetries of the as-built apparatus leads to a correction, A_{bias} , referred to as rescattering bias.

A schematic of the physical model for this effect is shown in Extended Data Fig. 3a. Scattered electrons, which are initially fully longitudinally polarized, acquire some transverse polarization through precession as they transport through the spectrometer's magnetic field.

The effect was modelled using a detailed Geant4⁵⁹ simulation of the transport of the detected electrons through the spectrometer and the Pb radiator, including electromagnetic showering and Mott scattering. An asymmetry in the distribution of electrons penetrating the radiator develops owing to the analysing power of low-energy Mott scattering. A possible analysing power for high-energy scattering due to non-Born processes⁶⁰ was also considered, but reasonable models for those processes⁶¹ showed a negligible contribution.

Asymmetries obtained from this simulation (and from a variety of analytic effective models that reproduced the key features of the simulation) were combined with scattered electron flux distributions and tailored parameterizations of the Cherenkov-light yield for each detector to estimate A_{bias} and its uncertainty. The light yield varied strongly with the arrival angle and position of the electron on the detector. The light-yield parameterizations were developed to match the observed light-yield distribution by tuning the optical parameters in a Geant4⁵⁹ optical-photon transport simulation. The largest systematic uncertainty was associated with the optical modelling of the individual as-built detectors. This uncertainty was determined from the range of predicted A_{bias} values, which was obtained by varying the optical parameters in the simulation while maintaining reasonable agreement with the measured light yield distributions. The predicted A_{bias} values for each detector are shown in Extended Data Fig. 3c. The resulting averaged correction and its systematic uncertainty are $A_{\text{bias}} = 4.3 \pm 3.0$ p.p.b.

This result was consistent to within 1 p.p.b. with a simpler, independent calculation based on a phenomenological approach, which used the measured position distributions of the electron flux on the pre-radiators and the measured dependence of the light seen by each PMT on the track position on the detectors. The results obtained using the measured distributions from the experiment's tracking system were compared with those obtained from the simulation. In this approach, the effect of the position differences was scaled to match the observed left/right asymmetry. The sensitivity to various models for the position dependence of the asymmetries was found to be small.

Determination of A_{ep} . The measured asymmetry A_{msr} was then corrected for incomplete beam polarization, the effects of various background processes, electromagnetic radiative corrections and the finite acceptance of the detector, to obtain the fully corrected electron-proton asymmetry A_{ep} , using:

$$A_{\text{ep}} = R_{\text{tot}} \frac{A_{\text{msr}}/P - \sum_{i=1,3,4} f_i A_i}{1 - \sum_{i=1,3,4} f_i} \quad (8)$$

where $R_{\text{tot}} = R_{\text{rc}} R_{\text{det}} R_{\text{acc}} R_{Q^2}$, f_i are dilutions to the signal and A_i are false or background process asymmetries. The components of equation (8) are discussed below.

(1) R_{rc} . The electromagnetic radiative correction factor $R_{\text{rc}} = 1.010 \pm 0.005$ accounts for the effect of internal and external bremsstrahlung of the incident electron, which can depolarize the electron and modify the momentum transfer Q^2 at the scattering vertex. R_{rc} was determined using a Geant3⁵⁹ simulation by comparing results with and without bremsstrahlung enabled in the simulation.

(2) R_{det} . The Cherenkov detector analogue response (that is, the summed optical signal detected by the two PMTs attached at each end of each detector) varied as a function of the arrival location of the scattered electron on the detector. The magnetic optics of the spectrometer also caused a correlation of the electron arrival location with Q^2 and, therefore, with the asymmetry. The correlation between the detector's analogue response and the Q^2 value of each track was determined using the tracking-system drift chambers, and the resulting correction to the measured asymmetry was $R_{\text{det}} = 0.9895 \pm 0.0021$.

(3) R_{acc} . Owing to the finite acceptance of the spectrometer and the effect of radiative energy losses, A_{msr} represents an average over a range of Q^2 values. Because the asymmetry varies strongly with Q^2 , we used a simulation to correct the averaged asymmetry $\langle A(Q^2) \rangle$ to the asymmetry that would arise from point scattering at the central $\langle Q^2 \rangle$, $A(\langle Q^2 \rangle)$, using:

$$R_{\text{acc}} = \frac{A(\langle Q^2 \rangle)}{\langle A(Q^2) \rangle} = 0.977 \pm 0.002$$

(4) R_{Q^2} . The central $\langle Q^2 \rangle$ for the experiment was determined from a Geant4 simulation that was benchmarked with measurements from the tracking system. The $\langle Q^2 \rangle$ value was not identical for Run 1 and Run 2 because of minor differences in the beam energy, target location and magnetic field of the spectrometer, with Run 1 having a higher $\langle Q^2 \rangle$. The global fit of A_{ep} versus Q^2 (see Fig. 2) was used to determine the sensitivity of the asymmetry to small changes in $\langle Q^2 \rangle$. Run 2 was chosen as the reference for $\langle Q^2 \rangle$, and the Run 1 asymmetry was scaled from its measured $\langle Q^2 \rangle$ value using $R_{Q^2} = 0.9928$ ($R_{Q^2} = 1$ for Run 2, by definition). The determination of the central $\langle Q^2 \rangle$ value has a 0.45% relative uncertainty, dominated by the uncertainties on the locations of the collimator, target and main detector and that of the beam energy determination. To simplify the global fitting, we decided to quote $\langle Q^2 \rangle$ as exact and used the sensitivity $\partial A_{\text{ep}} / \partial Q^2$ to determine an effective error contribution to the asymmetry. This error on R_{Q^2} was 0.0055 for both run periods. The acceptance-averaged Q^2 , scattering angle and incident electron energy were $\langle Q^2 \rangle = 0.0248 \text{ GeV}^2 c^{-2}$, $\langle \theta \rangle = 7.90^\circ$ and $\langle E_0 \rangle = 1.149 \text{ GeV}$, respectively.

(5) Beam polarization, P . To achieve a reliable determination of the beam polarization (P) at $<1\%$ accuracy, two different techniques with precisely calculated analysing powers were employed for redundancy. An existing Møller polarimeter⁶² in experimental Hall C was used invasively 2–3 times a week. It measured the parity-conserving cross-section asymmetry in the scattering of polarized beam electrons from polarized electrons in an iron foil target at low (typically smaller than or equal to $\sim 2 \mu\text{A}$) beam currents. A newly installed, non-invasive Compton polarimeter⁷ monitored the beam polarization continuously at the full-production beam current of $180 \mu\text{A}$. This device measured the parity-conserving asymmetry in the scattering of beam electrons from circularly polarized laser photons. For each run period, the averaged beam-polarization-corrected asymmetry was computed in two ways: by correcting each ~ 6 -min period of data-taking for the polarization measured during that interval, and by using an overall average beam polarization for the whole run period. Because the two methods gave the same result to a small fraction of the quoted uncertainty, for simplicity the results obtained using the overall average beam polarization are quoted here. The overall average beam polarizations for the two running periods were $P_{\text{Run1}} = (87.66 \pm 1.05)\%$ and $P_{\text{Run2}} = (88.71 \pm 0.55)\%$, where the uncertainties are predominantly systematic. For Run 1, the uncertainty was larger for two reasons: the Compton polarimeter was still being commissioned, so it was not used for this determination, and the Møller uncertainty was larger than usual owing to the need to correct for the effects of an intermittent short circuit in one of the quadrupole magnets of the polarimeter. For Run 2, both polarimeters were fully functional and agreed well with each other, as shown in Extended Data Fig. 4. A dedicated direct comparison of the Møller and Compton polarimeters under identical beam conditions at low beam current was also performed. The two techniques agreed within the uncertainties for that measurement, $dP/P = 1\%$ and $dP/P = 0.73\%$ for the Compton and Møller polarimeters, respectively⁶³.

Physics backgrounds (target windows). The entrance (0.11-mm-thick) and exit (0.13-mm-thick) windows of the hydrogen target were made of aluminium 7075 alloy. Electrons scattered from these windows caused the dominant background

process ($f_1 A_1 = 37$ p.p.b. for Run 1 and $f_1 A_1 = 38$ p.p.b. for Run 2). The parity-violating elastic asymmetry for electrons scattered from aluminium is observed to be nearly an order of magnitude larger than that for scattering from hydrogen owing to the much larger weak charge of the aluminium nucleus⁶⁴. Therefore, even the small fraction of the detected yield arising from the windows required a substantial correction to the measured asymmetry. The aluminium asymmetry was determined in dedicated data-taking runs using an aluminium target made from the same block of material as the target windows but with a thickness (3.7 mm) to match the radiation length of the hydrogen target. The ranges of scattering angles accepted from the upstream and downstream windows were different, which required a small kinematic correction to the measured alloy asymmetry to yield the asymmetry from the target windows $A_1 = 1.515 \pm 0.077$ p.p.m. (see Extended Data Fig. 5). The uncertainty is dominated by statistics but includes systematic uncertainties arising from the kinematic correction, among others. The fraction of the measured yield arising from the target windows, $f_1 = (2.471 \pm 0.056)\%$ (Run 1) and $f_1 = (2.516 \pm 0.059)\%$ (Run 2), was measured with a low beam current on an evacuated target cell, and a simulation was used to correct for radiative effects due to the liquid hydrogen.

Physics backgrounds (beamline background dilution). As described above (see 'Beamline-background asymmetry correction, A_{bb} '), a component of the background came from scattering sources in the beamline. The dilution from this source was measured⁵⁸ to be $f_2 = (0.193 \pm 0.064)\%$ by blocking two of the eight openings in the first collimator to eliminate the electron elastic-scattering signal from the target. The uncertainty accounts for variation in the f_2 value between detectors and under different beam conditions.

Physics backgrounds (neutral background). A possible contribution from low-energy neutral backgrounds arising from secondary interactions of the primary scattered electrons in the collimators and magnet structure was bounded⁶⁵ to $f_3 < 0.30\%$ by subtracting f_2 from the total neutral background measured by the main detector after vetoing charged particles using thin scintillators. The asymmetry for this background was estimated⁶⁵ from a Geant4⁵⁹ simulation of the contributing processes to be $A_3 = -0.39 \pm 0.16$ p.p.m., with the dominant contribution coming from secondary interactions of electrons elastically scattered from protons.

Physics backgrounds (inelastic electrons). An unavoidable background component comes from inelastically scattered electrons that have excited the target protons to the $\Delta(1232)$ resonance, a small fraction of which enter the acceptance of the spectrometer. The fraction of the yield from inelastically scattered electrons was estimated using simulation to be $f_4 = (1.82 \pm 0.37) \times 10^{-4}$. To determine the correction to the asymmetry owing to these events, we measured the parity-violating asymmetry in the energy region near the $\Delta(1232)$ resonance during a dedicated study with a reduced spectrometer current to concentrate these electrons on the detectors. Scaling this asymmetry up to the Q^2 value of the elastic peak gives an inelastic asymmetry of $A_4 = -3.0 \pm 1.0$ p.p.m. at the elastic peak. Backgrounds from π^- particles and other hadrons were negligible.

Summary of corrections to the asymmetry and their uncertainties. The separate and combined measured asymmetries for Runs 1 and 2 are presented in Extended Data Table 2. Also shown is the breakdown of these uncertainties in terms of descending fractional significance. Extended Data Table 3 presents the numerical values of the raw asymmetry, A_{raw} , along with all systematic and acceptance correction factors used to derive the observed measured asymmetry, A_{msr} , and physics asymmetries, A_{ep} , using equations (7) and (8). Correlated uncertainties, accounted for when the two runs were combined, are also listed.

The fully corrected asymmetry is $A_{\text{ep}} = -223.5 \pm 15.0$ (statistical) ± 10.1 (systematic) p.p.b. for Run 1 and $A_{\text{ep}} = -227.2 \pm 8.3$ (statistical) ± 5.6 (systematic) p.p.b. for Run 2. The combined asymmetry is $A_{\text{ep}} = -226.5 \pm 7.3$ (statistical) ± 5.8 (systematic) p.p.b.

Data quality. Two representative tests of the consistency and the quality of the corrected asymmetries are presented below.

Null result. The Q_{weak} experiment employed signal phase locking on three independent techniques of polarized-beam helicity reversal that were used to isolate the scattering asymmetry. These were the rapid (960 Hz) reversal, the insertion of a half-wave plate in the source laser optical path at 8-h intervals and the Wien-filter reversal at monthly intervals. The half-wave plate technique is based on a mechanical action and thus is unable to induce any false asymmetries electrically or magnetically. The Wien-filter reversal rejects false asymmetries induced by beam-size (or focus) modulation. By constructing an out-of-phase, or null, asymmetry A_{null} from the latter two slow-reversal techniques, we can determine whether there are unaccounted-for false asymmetries. The full dataset-weighted null is $A_{\text{null}} = -1.75 \pm 6.51$ p.p.b., which is consistent with zero, as expected.

Asymmetry measurements. A plot of the observed main-detector asymmetry versus the Wien-filter configuration is shown in Extended Data Fig. 6. Run 1 and Run 2 were separated by a six-month accelerator shutdown, during which numerous modifications were made to the experimental apparatus and accelerator. These included upgrading the electronics associated with the beam current measurement

and increasing the number of associated BCMs. An electrically isolated helicity phase-locked beam-position stabilization system was enabled in the 6-MeV region of the injector during Run 2. This greatly improved the helicity-correlated stability of the beam delivered to the experiment. There were also radio-frequency-associated electronics and superconducting-cavity upgrades performed within the accelerator, unrelated to this experiment, as well as extensive upgrades to both beam polarimeters. As a consequence, the contributions of many beam-related systematic effects meaningfully changed between the two run periods. However, the resulting fully corrected physics asymmetries of the two run periods agree well. This is evidence that within the experiment's precision, the observed set of identified systematic effects is complete and their associated correction algorithms behave in a deterministic manner.

Electroweak radiative corrections and extraction of $\sin^2\theta_W$. The weak mixing angle is obtained from the proton's weak charge, taking into account energy-independent electroweak radiative corrections using¹

$$4\sin^2\theta_W(0) = 1 - \frac{Q_W^p - \square_{WW} - \square_{ZZ} - \square_{\gamma Z}(0)}{(\rho + \Delta_e)} + \Delta'_e \quad (9)$$

Here, \square_{WW} and \square_{ZZ} are the WW and ZZ boson box-diagram radiative corrections, ρ is the renormalization of the ratio of neutral-current (Z^0) to charged-current (W^\pm) interactions at low energy, Δ_e is the electron vertex correction to the axial Zee interaction, Δ'_e is the electron anapole moment and $\square_{\gamma Z}(0)$ refers to the remaining energy-independent piece of the γZ -box diagram (the energy-dependent piece was discussed in 'Global fit').

The accidental suppression of the proton's weak charge in the standard model means that Q_W^p is unusually sensitive to $\sin^2\theta_W$. To see this quantitatively, our determination of Q_W^p to a precision of 6.25% results in a $\sin^2\theta_W$ precision of 0.46%. By contrast, the higher relative precision (0.59%) of the weak charge measurement^{14,15} on ¹³³Cs, which is dominated by the neutron's weak charge, which is not suppressed in the standard model, leads to a $\sin^2\theta_W$ uncertainty of 0.81%, almost twice the uncertainty of our result.

The radiative corrections appearing in equation (9) are described in ref.¹ but were re-evaluated using the more recent input found in refs.^{2,11}. Although Q_W^p in equation (6) is defined in the Thomson limit ($Q \ll m_e$, where m_e is the electron mass) at $Q=0$, it is determined from data in the scattering limit ($Q \gg m_e$). We chose to use radiative corrections in the Thomson limit from ref. 1 to calculate $\sin^2\theta_W(0)$ from Q_W^p . Extended Data Table 4 lists these corrections^{1,2,11,67}.

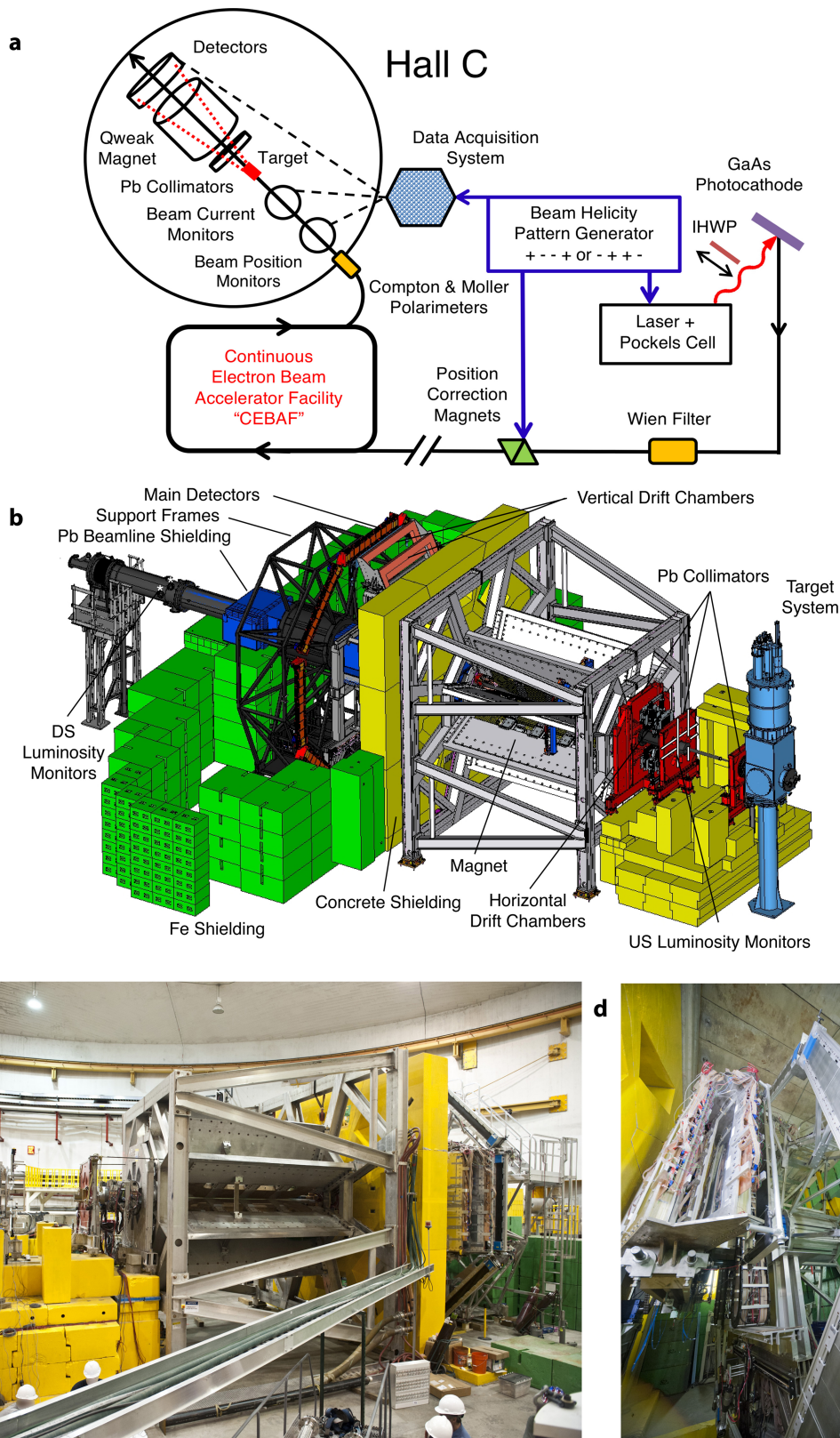
To compare our result for $\sin^2\theta_W(0)$, given by equation (9), with that of refs.^{2,34}, we added a correction of $2\alpha/(9\pi)$, consistent with the definition of ref.⁶⁶, as discussed in ref.²⁰. The result is $\sin^2\theta_W(Q=0) = 0.2384 \pm 0.0011$ in the \overline{MS} scheme². Shifting this to the $Q=0.158$ GeV of the Q_{weak} experiment (a correction of -0.00012), our result is $\sin^2\theta_W(Q=0.158 \text{ GeV}) = 0.2382 \pm 0.0111$.

Data availability. The 200 TB of raw data acquired in this work are stored at the Jefferson Laboratory data silo. The derived data supporting the findings of this study are available from the corresponding authors upon request.

Code availability. The software used for data management and analysis consisted of commercial and publicly available codes, plus experiment-specific software. Jefferson Laboratory's data management plan is available at <https://scicomp.jlab.org/DataManagementPlan.pdf>. The experiment-specific software is stored in a version management system (SVN & GIT) and archived at the data storage facilities of Jefferson Laboratory, in accordance with existing US regulations. Requests for this material should be addressed to the corresponding authors.

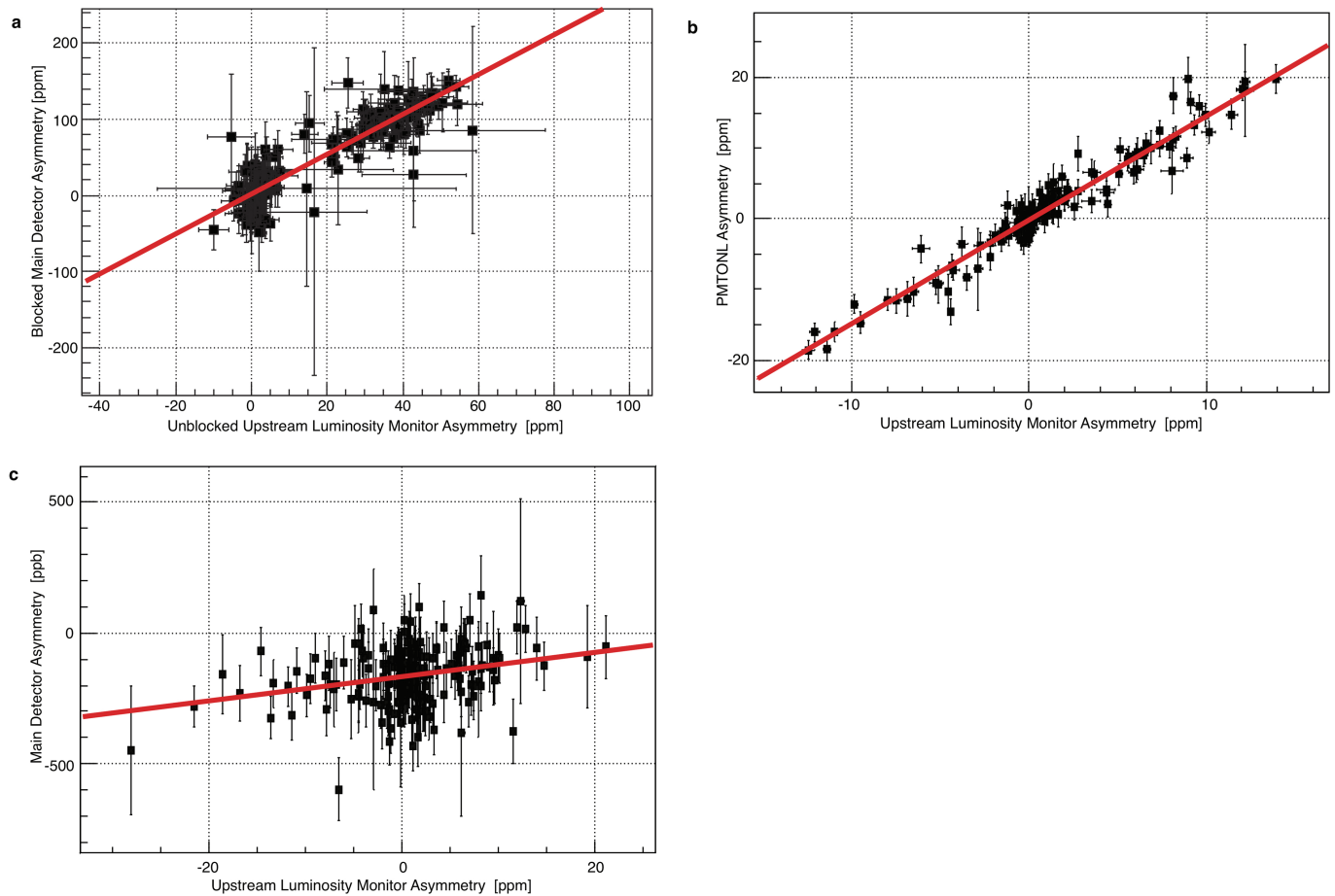
33. Musolf, M. J. et al. Intermediate-energy semileptonic probes of the hadronic neutral current. *Phys. Rep.* **239**, 1–178 (1994).
34. Erler, J. & Ramsey-Musolf, M. J. Low energy tests of the weak interaction. *Prog. Part. Nucl. Phys.* **54**, 351–442 (2005).
35. Armstrong, D. S. & McKeown, R. D. Parity-violating electron scattering and the electric and magnetic strange form factors of the proton. *Annu. Rev. Nucl. Part. Sci.* **62**, 337–359 (2012).
36. GO Collaboration. Strange quark contributions to parity-violating asymmetries in the forward GO electron-proton scattering experiment. *Phys. Rev. Lett.* **95**, 092001 (2005).

37. GO Collaboration. Strange quark contributions to parity-violating asymmetries in the backward angle GO electron scattering experiment. *Phys. Rev. Lett.* **104**, 012001 (2010).
38. HAPPEX Collaboration. Parity-violating electroweak asymmetry in ep scattering. *Phys. Rev. C* **69**, 065501 (2004).
39. HAPPEX Collaboration. Constraints on the nucleon strange form-factors at $Q^2 \sim 0.1 \text{ GeV}^2$. *Phys. Lett. B* **635**, 275–279 (2006).
40. HAPPEX Collaboration. Precision measurements of the nucleon strange form factors at $Q^2 \sim 0.1 \text{ GeV}^2$. *Phys. Rev. Lett.* **98**, 032301 (2007).
41. HAPPEX Collaboration. New precision limit on the strange vector form factors of the proton. *Phys. Rev. Lett.* **108**, 102001 (2012).
42. Spayde, D. T. et al. The strange quark contribution to the proton's magnetic moment. *Phys. Lett. B* **583**, 79–86 (2004).
43. Maas, F. E. et al. Measurement of strange quark contributions to the nucleon's form-factors at $Q^2 = 0.230 \text{ (GeV/c)}^2$. *Phys. Rev. Lett.* **93**, 022002 (2004).
44. Maas, F. E. et al. Evidence for strange quark contributions to the nucleon's form-factors at $Q^2 = 0.108 \text{ (GeV/c)}^2$. *Phys. Rev. Lett.* **94**, 152001 (2005).
45. Baunack, S. et al. Measurement of strange quark contributions to the vector form factors of the proton at $Q^2 = 0.22 \text{ (GeV/c)}^2$. *Phys. Rev. Lett.* **102**, 151803 (2009).
46. HAPPEX Collaboration. Parity-violating electron scattering from ⁴He and the strange electric form factor of the nucleon. *Phys. Rev. Lett.* **96**, 022003 (2006).
47. Balaguer Ríos, D. et al. Measurement of the parity violating asymmetry in the quasielastic electron-deuteron scattering and improved determination of the magnetic strange form factor and the isovector anapole radiative correction. *Phys. Rev. D* **94**, 051101 (2016).
48. SAMPLE Collaboration. Parity violating electron deuteron scattering and the proton's neutral weak axial vector form-factor. *Phys. Rev. Lett.* **92**, 102003 (2004).
49. González-Jiménez, R., Caballero, J. A. & Donnelly, T. W. Global analysis of parity-violating asymmetry data for elastic electron scattering. *Phys. Rev. D* **90**, 033002 (2014).
50. Zhu, S., Puglia, S. J., Holstein, B. R. & Ramsey-Musolf, M. J. Nucleon anapole moment and parity-violating ep scattering. *Phys. Rev. D* **62**, 033008 (2000).
51. Kelly, J. J. Simple parametrization of nucleon form factors. *Phys. Rev. C* **70**, 068202 (2004).
52. Galster, S., Klein, H., Moritz, J., Schmidt, K. H. & Wegener, D. Elastic electron-deuteron scattering and the electric neutron form factor at four momentum transfers $5 \text{ fm}^{-2} < q^2 < 14 \text{ fm}^{-2}$. *Nucl. Phys. B* **32**, 221–237 (1971).
53. Venkat, S., Arrington, J., Miller, G. A. & Zhan, X. Realistic transverse images of the proton charge and magnetic densities. *Phys. Rev. C* **83**, 015203 (2011).
54. Rislw, B. C. & Carlson, C. E. Modification of electromagnetic structure functions for the γZ -box diagram. *Phys. Rev. D* **88**, 013018 (2013).
55. Grame, J. et al. Two Wien filter spin flipper. In *Proc. 2011 Particle Accelerator Conference* (eds Satogata, T. & Brown, K.) 862–864 (IEEE, New York, 2011).
56. Arrington, J., Blunden, P. G. & Melnitchouk, W. Review of two-photon exchange in electron scattering. *Prog. Part. Nucl. Phys.* **66**, 782–833 (2011).
57. Qweak Collaboration. Beam normal single spin asymmetry measurements from Q_{weak} . Preprint at <https://arxiv.org/abs/1604.04602> (2016).
58. Kargiantoulakis, E. *A Precision Test of the Standard Model via Parity-Violating Electron Scattering in the Q_{weak} Experiment*. PhD thesis, Univ. Virginia (2015); https://misportal.jlab.org/ul/publications/view_publication?pub_id=14261.
59. Agostinelli, S. et al. Geant4 – a simulation toolkit. *Nucl. Instrum. Meth. A* **506**, 250–303 (2003).
60. Abrahamyan, S. et al. New measurements of the transverse beam asymmetry for elastic electron scattering from selected nuclei. *Phys. Rev. Lett.* **109**, 192501 (2012).
61. Gorchtein, M. & Horowitz, C. J. Analyzing power in elastic scattering of the electrons off a spin-0 target. *Phys. Rev. C* **77**, 044606 (2008).
62. Hauger, M. et al. A high-precision polarimeter. *Nucl. Instrum. Meth. A* **462**, 382–392 (2001).
63. Magee, J. et al. A novel comparison of Møller and Compton electron-beam polarimeters. *Phys. Lett. B* **766**, 339–344 (2017).
64. Horowitz, C. J. Parity violating elastic electron scattering from ²⁷Al and the QWEAK measurement. *Phys. Rev. C* **89**, 045503 (2014).
65. McHugh, M. *A Measurement of the Transverse Asymmetry in Forward-Angle Electron-Carbon Scattering Using the Q_{weak} Apparatus*. PhD thesis, George Washington Univ. (2017); https://misportal.jlab.org/ul/publications/view_publication?pub_id=14918.
66. Ferroglia, A., Ossola, G. & Sirlin, A. Bounds on M_W , M_t , $\sin^2\theta_{\text{eff}}^{\text{lept}}$. *Eur. Phys. J. C* **35**, 501–507 (2004).
67. Bethke, S. *as 2002. Nucl. Phys. B Proc. Sup.* **121**, 74–81 (2003).



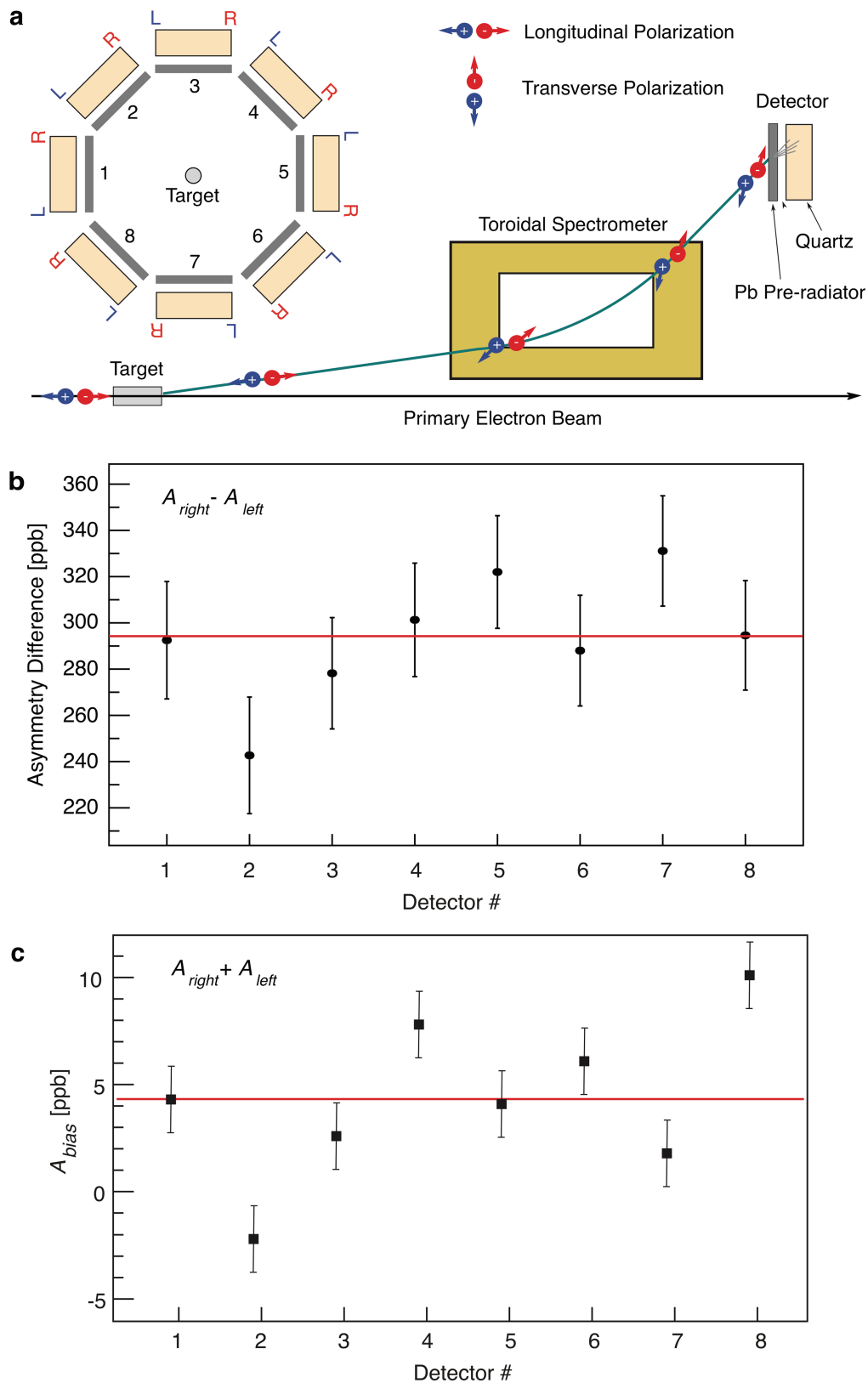
Extended Data Fig. 1 | Apparatus. **a**, Schematic of critical accelerator components and the Q_{weak} apparatus⁴. The electron beam is generated at the photocathode, accelerated by the Continuous Electron Beam Accelerator Facility (CEBAF) and sent to experimental Hall C, where it is monitored by beam position monitors and beam current monitors. The insertable half-wave plate (IHWP) provides slow reversal of the electron

beam helicity. The data acquisition system records the data. **b**, Computer-aided design drawing of the experimental apparatus. **c**, The Q_{weak} apparatus, before the final shielding configuration was installed. **d**, Interior of the hut shielding the detectors, showing two of the Cherenkov detectors (right) and a pair of tracking chambers (left).



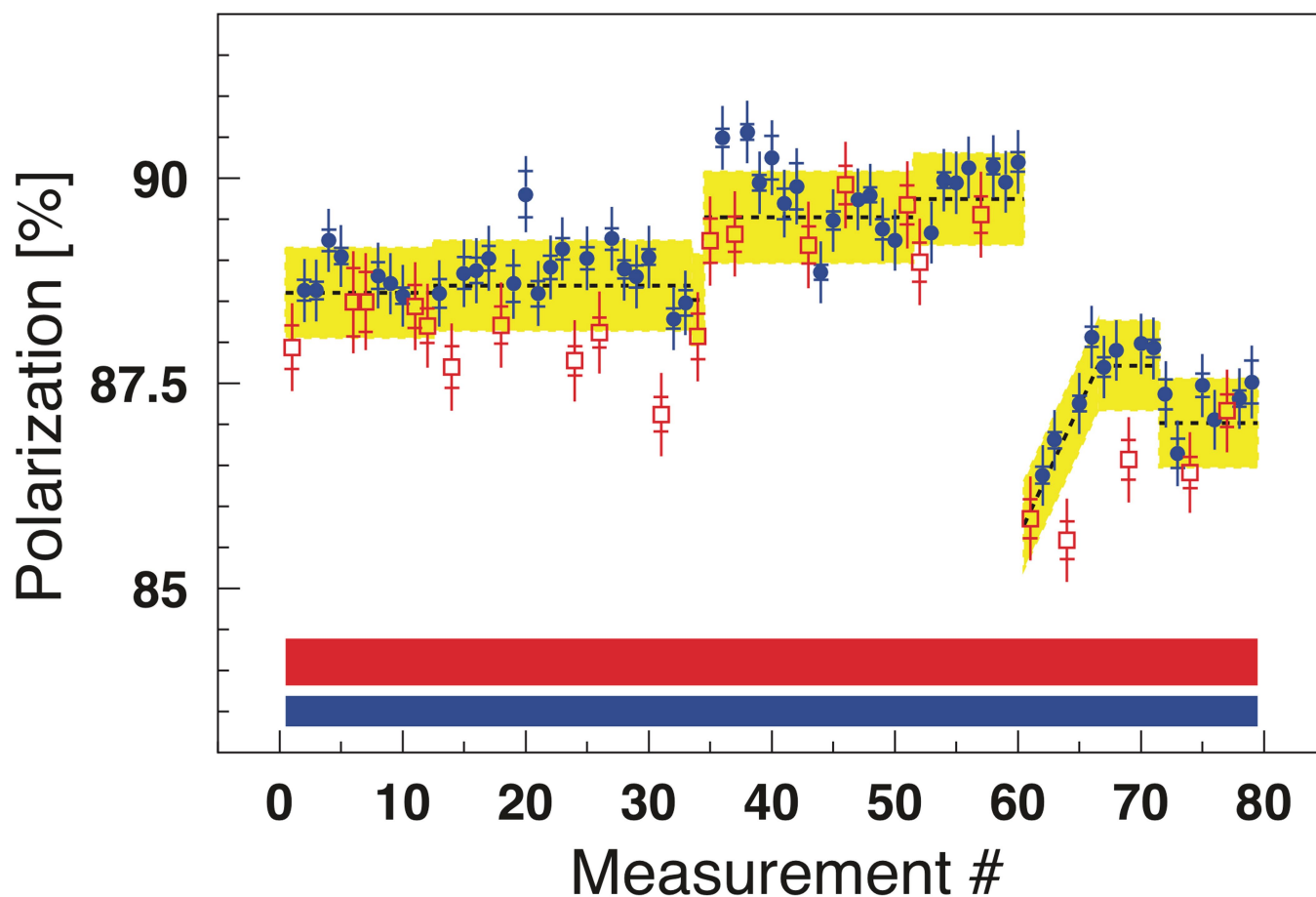
Extended Data Fig. 2 | Beamline background. Determination of A_{bb} , the false asymmetry arising from beamline background events. Uncertainties are 1 s.d. **a**, Correlation of the main detector asymmetry to that of the upstream luminosity monitors, measured when the signal from elastically scattered electrons in the main detectors was blocked at the first

collimator. **b**, Correlation of asymmetries from the upstream luminosity monitors with one of the other background detectors (a bare PMT located in the detector shield house). **c**, Correlation of the unblocked main detector asymmetry to that of the upstream luminosity monitor for Run 2. Our A_{bb} determination was based on this slope.



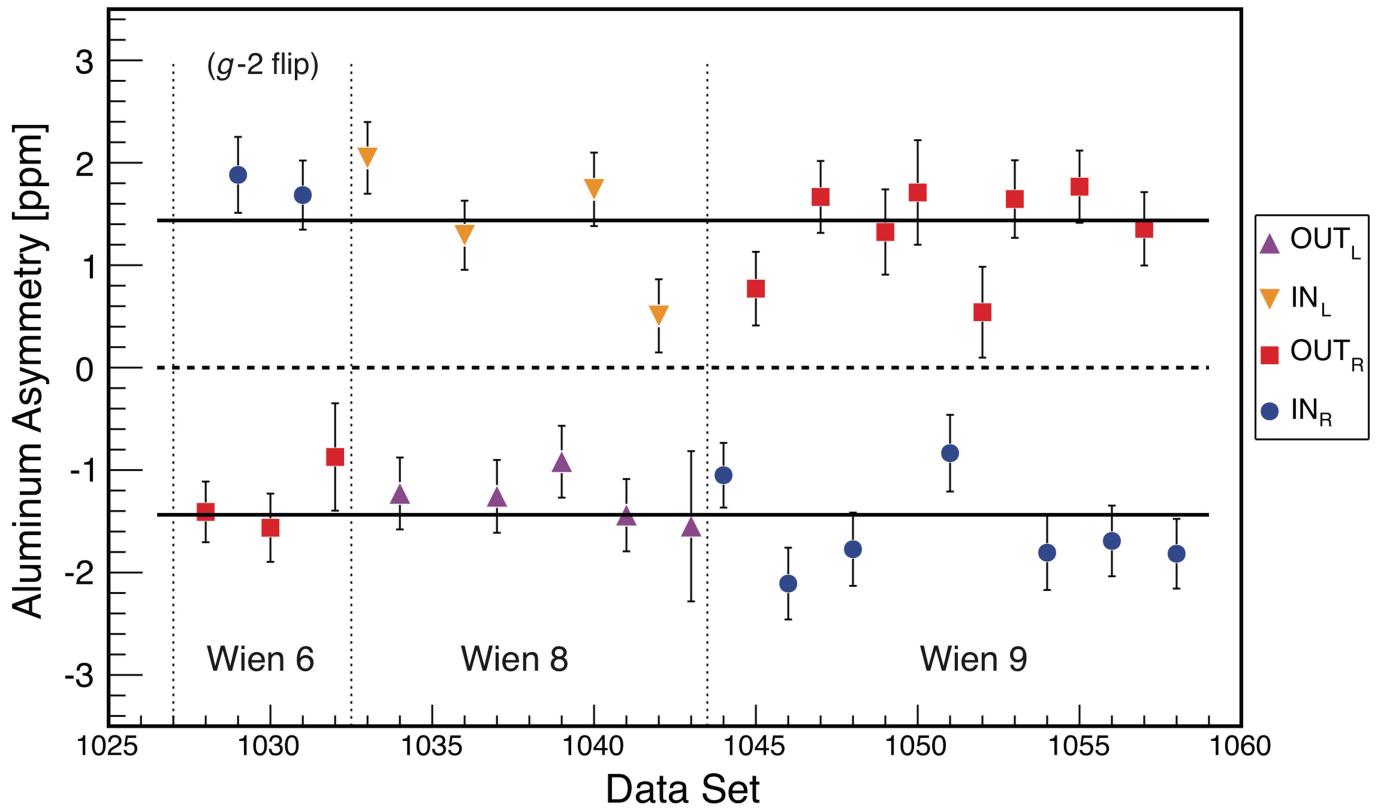
Extended Data Fig. 3 | Rescattering bias. **a**, Schematic illustrating the precession of longitudinally polarized electrons through the spectrometer magnet, generating sizeable transverse spin components upon arrival at the detector array (spin directions indicated by red and blue arrows for the two electron helicity states). An end-view of the detector array, indicating

the right (R) and left (L) PMT positions, is shown on the left. **b**, Difference between the asymmetry measured by the two (R and L) PMT tubes versus the detector number (Run 2 data). **c**, Calculated rescattering bias A_{bias} versus detector number, with the eight-detector-averaged value shown by the red lines. Uncertainties (1 s.d.) are systematic.



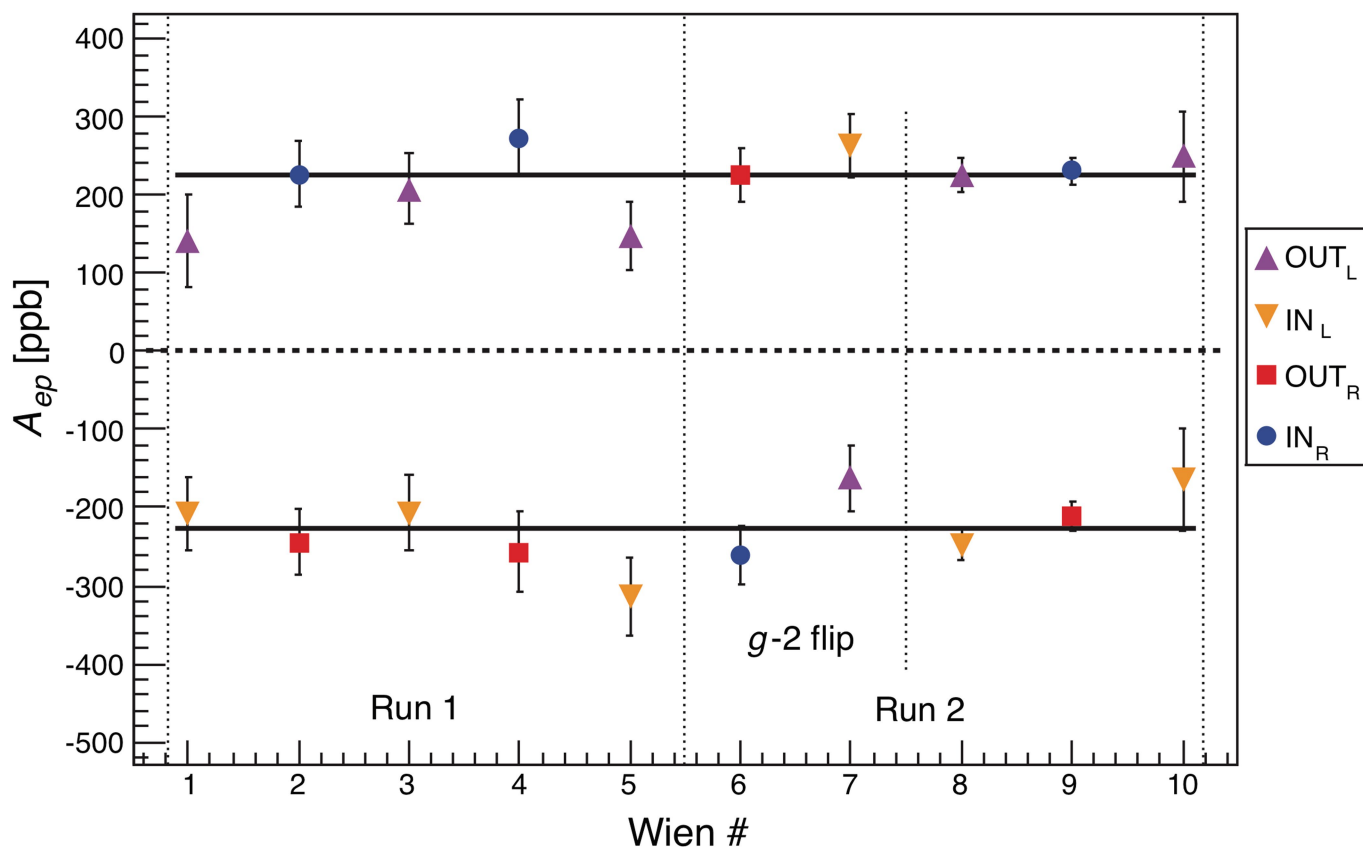
Extended Data Fig. 4 | Electron beam polarization. Measurements from the Compton (closed blue circles) and Møller (open red squares) polarimeters during Run 2. Inner error bars denote statistical uncertainties and outer error bars show the statistical and point-to-point systematic uncertainties added in quadrature. Normalization, or scale-type, uncertainties are shown by the solid blue (Compton) and red (Møller) bands. All uncertainties are 1 s.d. The yellow band shows the derived

polarization values used in the evaluation of the parity-violating asymmetry A_{ep} . The time dependence of the reported polarization is driven primarily by the continuous Compton measurements, with a small-scale correction (0.21%, not included in this figure) determined from an uncertainty-weighted global comparison of the Compton and Møller polarimeters.



Extended Data Fig. 5 | Asymmetry from aluminium. Parity-violating asymmetry from the aluminium alloy target versus the dataset number. All uncertainties are 1 s.d. The labels 'IN' and 'OUT' refer to the state of the insertable half-wave plate at the electron source, which generated a 180° flip of the electron spin when IN. The subscripts denote the setting of the Wien filter, with L and R corresponding to the presence and absence, respectively, of an additional 180° rotation of the spin direction of the electron beam. A period in which a further 180° flip was

generated through $(g_e - 2)$ precession (g_e , electron gyromagnetic ratio) via a modified accelerator configuration during Wien 6 is indicated. The combinations OUT-R and IN-L with no $(g_e - 2)$ spin flip reveal the physical sign of the asymmetry. Solid lines represent the time-averaged values, and the horizontal dashed line indicates zero asymmetry. The vertical dashed lines delineate particular data subsets with a given Wien filter setting.



Extended Data Fig. 6 | Asymmetry from the proton. Observed parity-violating asymmetry A_{ep} after all corrections, versus the dataset number (acquired in the double-Wien-filter configuration). The Wien filter reversed the beam helicity at approximately monthly intervals. The subscripts denote the setting of the Wien filter as L or R, corresponding to the presence or absence, respectively, of a 180° rotation of the spin direction of the electron beam. IN and OUT refer to the state of the insertable half-wave plate at the electron source, generating an additional 180° flip of the spin when IN. A period in which a further 180° flip was generated through $(g_e - 2)$ precession via a modified accelerator

configuration is indicated. The combinations OUT-R and IN-L with no $(g_e - 2)$ flip reveal the physical sign of the asymmetry. Solid lines represent the time-averaged values and the dashed line indicates zero asymmetry. The uncertainties (1 s.d.) shown are those of the corresponding A_{msr} values (see text) only—that is, they do not include time-independent uncertainties—so as to illustrate the time stability of the results. The weighted mean and P -value of the upper OUT-L and IN-R data are 226.9 ± 10.2 , $P = 0.59$ (upper solid line), respectively. For the opposite combination, OUT-R and IN-L, we find a weighted mean of -226.1 ± 10.5 and $P = 0.36$ (lower solid line).

Extended Data Table 1 | Helicity-correlated beam parameter differences and sensitivities

Beam Parameter	Run 1 $\Delta\chi_i$	Run 2 $\Delta\chi_i$	Typical $\partial A/\partial\chi_i$
X	-3.5 ± 0.1 nm	-2.3 ± 0.1 nm	-2 ppb/nm
X'	-0.30 ± 0.01 nrad	-0.07 ± 0.01 nrad	50 ppb/nrad
Y	-7.5 ± 0.1 nm	0.8 ± 0.1 nm	< 0.2 ppb/nm
Y'	-0.07 ± 0.01 nrad	-0.04 ± 0.01 nrad	< 3 ppb/nrad
Energy	-1.69 ± 0.01 ppb	-0.12 ± 0.01 ppb	-6 ppb/ppb

The beam parameter differences and typical detector sensitivities for the five measured beam parameters for Run 1 and Run 2. Uncertainties are 1 s.d.

Extended Data Table 2 | Asymmetries and their corrections

Period	Asymmetry (ppb)	Stat. Unc. (ppb)	Syst. Unc. (ppb)	Tot. Uncertainty (ppb)
Run 1	-223.5	15.0	10.1	18.0
Run 2	-227.2	8.3	5.6	10.0
Run 1 and 2 combined with correlations	-226.5	7.3	5.8	9.3

Quantity	Run 1 error (ppb)	Run 1 fractional	Run 2 error (ppb)	Run 2 fractional
BCM Normalization: A_{BCM}	5.1	25%	2.3	17%
Beamline Background: A_{BB}	5.1	25%	1.2	5%
Beam Asymmetries: A_{beam}	4.7	22%	1.2	5%
Rescattering bias: A_{bias}	3.4	11%	3.4	37%
Beam Polarization: P	2.2	5%	1.2	4%
Target windows: A_1	1.9	4%	1.9	12%
Kinematics: R_{Q^2}	1.2	2%	1.3	5%
Total of others	2.5	6%	2.2	15%
Combined in quadrature	10.1		5.6	

Top, corrected asymmetries A_{ep} for the Run 1 and Run 2 datasets, and the combined value, with their statistical (Stat. Unc.), systematic (Syst. Unc.) and total (Tot.) uncertainties (1 s.d.), in parts per billion (ppb). Bottom, fractional quadrature contributions $(\sigma_i/\sigma_{\text{tot}})^2$ to the systematic uncertainty (1 s.d.) on A_{ep} for Run 1 and Run 2. Only error sources with fractional contribution $\geq 5\%$ in one of the runs are shown.

Extended Data Table 3 | Raw asymmetries and their corrections

Quantity	Run 1	Run 2	Correlation
A_{raw}	-192.7 ± 13.2 ppb	-170.7 ± 7.3 ppb	—
A_{T}	0 ± 1.1 ppb	0 ± 0.7 ppb	0
A_{L}	1.3 ± 1.0 ppb	1.2 ± 0.9 ppb	1
A_{BCM}	0 ± 4.4 ppb	0 ± 2.1 ppb	0.67
A_{BB}	3.9 ± 4.5 ppb	-2.4 ± 1.1 ppb	0
A_{beam}	18.5 ± 4.1 ppb	0.0 ± 1.1 ppb	0
A_{bias}	4.3 ± 3.0 ppb	4.3 ± 3.0 ppb	1
A_{msr}	-164.6 ± 15.5 ppb	-167.5 ± 8.4 ppb	—
P	87.66 ± 1.05 %	88.71 ± 0.55 %	0.19
f_1	2.471 ± 0.056 %	2.516 ± 0.059 %	1
A_1	1.514 ± 0.077 ppm	1.515 ± 0.077 ppm	1
f_2	0.193 ± 0.064 %	0.193 ± 0.064 %	1
f_3	0.12 ± 0.20 %	0.06 ± 0.12 %	1
A_3	-0.39 ± 0.16 ppm	-0.39 ± 0.16 ppm	1
f_4	0.018 ± 0.004 %	0.018 ± 0.004 %	1
A_4	-3.0 ± 1.0 ppm	-3.0 ± 1.0 ppm	1
R_{RC}	1.010 ± 0.005	1.010 ± 0.005	1
R_{Det}	0.9895 ± 0.0021	0.9895 ± 0.0021	1
R_{Acc}	0.977 ± 0.002	0.977 ± 0.002	1
R_{Q^2}	0.9928 ± 0.0055	1.0 ± 0.0055	1
R_{tot}	0.9693 ± 0.0080	0.9764 ± 0.0080	1
$\sum f_i$	2.80 ± 0.22 %	2.78 ± 0.15 %	1

The raw measured asymmetries A_{raw} for the two run periods, and all the corrections (including for false asymmetries, backgrounds, beam polarization and detector acceptance) that were applied to extract the final asymmetry A_{ep} from A_{raw} (see text). The f_i values are dilutions to the signal, A_i are false or background process asymmetries, P is the beam polarization and R_i are multiplicative factors. The net multiplicative correction R_{tot} and the total dilution are also indicated, as well as the values of A_{msr} , the asymmetry after the corrections for the false asymmetries (see equation (7)). The correlations used to combine the two runs are provided in the final column. Uncertainties are 1 s.d.

Extended Data Table 4 | Radiative corrections

Term	Expression	Value	Reference
ρ_{NC}	$1 + \Delta_\rho$	1.00066	1, 2
Δ_e	$-\alpha/2\pi$	-0.001161	1, 2
Δ'_e	$-\frac{\alpha}{3\pi}(1 - 4\hat{s}^2) \left[\ln \left(\frac{M_Z^2}{m_e^2} \right) + \frac{1}{6} \right]$	-0.001411	1, 2
$\hat{\alpha}$	$\equiv \alpha(M_Z)$	1/127.95	1, 2
\hat{s}^2	$= 1 - \hat{c}^2 \equiv \sin^2 \theta_W(M_Z)$	0.23129	1, 2
$\alpha_s(M_W^2)$	-	0.12072	67
\square_{WW}	$\frac{\hat{\alpha}}{4\pi\hat{s}^2} \left[2 + 5 \left(1 - \frac{\alpha_s(M_W^2)}{\pi} \right) \right]$	0.01831	1, 2
\square_{ZZ}	$\frac{\hat{\alpha}}{4\pi\hat{s}^2\hat{c}^2} [9/4 - 5\hat{s}^2] (1 - 4\hat{s}^2 + 8\hat{s}^2) \left(1 - \frac{\alpha_s(M_Z^2)}{\pi} \right)$	0.00185	1, 2
$\square_{\gamma Z}$	axial-vector hadron piece of $\square_{\gamma Z}$: $\Re \square_{\gamma Z}^A$	0.0044	11

Numerical values used for the electroweak radiative corrections in equation (9).